https://doi.org/10.5194/gmd-2021-358
Preprint. Discussion started: 22 November 2021

Geoscientific Model Development Discussions
Open Access
EGU

On the application and grid-size sensitivity of the urban dispersion model CAIRDIO for the simulation of a real city and realistic meteorology.

Michael Weger[1], Bernd Heinold[1], Alfred Wiedensohler[1], and Maik Merkel[1]
[1]Leibniz Institute for Tropospheric Research, Leipzig, Germany
Correspondence: Michael Weger (weger@tropos.de)

Abstract. There is a gap between the need for city-wide air-quality simulations considering the intra-urban variability and mircoscale dispersion features and the computational capacities that conventional urban microscale models require. This gap can be bridged by targeting model applications on the gray zone situated between the mesoscale and large-eddy scale. The urban dispersion model CAIRDIO is a new contribution to the class of computational-fluid dynamics models operating in this scale range. It uses a diffuse-obstacle boundary method to represent buildings as physical obstacles at gray-zone resolutions in the order of tens of meters. The main objective of this approach is to find an acceptable compromise between computationally inexpensive grid sizes for spatially comprehensive applications and the required accuracy in the description of building and boundary-layer effects. For this purpose, CAIRDIO is applied in dispersion simulation of black carbon and particulate matter for an entire mid-size city using an uniform horizontal resolution of $40\,\mathrm{m}$ in this paper. For evaluation, the simulation results are compared with measurements from 5 operational air monitoring stations, which are representative for the urban background and high-traffic roads, respectively. Moreover, the comparison includes the mesoscale host simulation, which provides the boundary conditions. The temporal variability of the concentration measurements at the background sites was largely influenced only by the characteristics of the mixing layer. As a consequence, the model results were not significantly dependent on spatial resolution, so that the mesoscale simulation also performed reasonably well. At the traffic sites, however, concentrations were in addition markedly influenced by the proximity to road-traffic sources and the surrounding building environment. Here, the mesoscale simulation indiscriminately reproduced almost the same urban-background profiles, which resulted in a large positive model bias. On the other hand, the CAIRDIO simulation was able to respond to the significantly amplified diurnal variability with its pronounced rush-hour peaks. This resulted in a consistent improvement of the model deviation to measurements compared to the mesoscale simulation. Nevertheless, discrepancies to measurements remain in the $40\,\mathrm{m}$-CAIRDIO simulation, e.g., an underestimation of peak concentrations at two traffic sites inside narrow street canyons. To further research resolution sensitivity, the horizontal grid spacing of locally nested CAIRDIO domains is refined down to $5\,\mathrm{m}$. While for the street canyons the representation of peak concentrations can be improved using horizontal grid spacings of up to $10\mathrm{m}$, no further improvements beyond this resolution can be observed. This suggests that the too low peak concentrations with the default grid spacing of $40\,\mathrm{m}$ result from an inadequate representation of the traffic emissions inside narrow street canyons. If the total gain in accuracy due to the grid refinements is put in relation to the remaining model error, the improvements are only modest.

https://doi.org/10.5194/gmd-2021-358
Preprint. Discussion started: 22 November 2021


Geoscientific Model Development Discussions

In conclusion, the proposed gray-scale modeling is a promising downscaling approach for urban air-quality applications. Nevertheless, the results also show that aspects other than the actual resolution of flow patterns and numerical effects can determine the simulations at the urban microscale.

1 Introduction

Air pollution from particulate matter (PM) is a major risk factor to population health and is estimated to contribute to at least 8 million premature deaths annually (Burnett et al., 2018; Vohra et al., 2021). For Europe, similar figures estimate the annual mortality excess by up to 900,000 (Tarín-Carrasco et al., 2021), thus health-adverse air quality conditions remain an issue also in well-developed countries. Despite continued efforts in emission reductions and an associated decline in $PM_{2.5}$ concentrations over the past decades (Ortiz and Guerreiro, 2020), the associated mortality risk has only slowly responded to it, and it may increase again in the future due to projected changes in demographics and climate in an adverse way to increase population vulnerability (Sicard et al., 2021). The burden on human health from air pollution is especially relevant for urban areas, not only because more than half of the global population resides there. Urban emissions from traffic and industrial locations locally contribute to a large extend to the primary particulate matter (PPM) fraction, which is most hazardous to human health (Park et al., 2018). Important health-relevant constituents are black-carbon (BC), organic carbon (OC) and road dust. PPM typically exhibits high concentrations close to sources, rapidly decreasing with increased distance, and thus also largely determines the intra-urban variability of PM (Wu et al., 2015). On the other hand, secondary particulate matter (SPM) is formed within the atmosphere from precursor compounds, is generally considered less toxic (Park et al., 2018), and transport is more relevant at the regional scale (Ying et al., 2021), thus taking effect as a near-constant offset in PM concentrations at the intra-urban scale. Aside from the mere location of sources, the effect of the urban canopy on pollutant dispersion is a crucial factor in the characteristic of the intra-urban variability of air pollution (Brown et al., 2015). Buildings affect pollution dispersion across multiple scales through mechanical and thermal interactions with the air flow, which are often too complex to be described in a general way (Roth, 2000). As a consequence, a large pool of literature exists on this topic. Studies investigating such effects are either based on experimental observations, physical models, numerical simulations or combined approaches of varying complexity. To mention few examples, studies have been carried out for isolated buildings (Higson et al., 1996; Foroutan et al., 2018; Jiang and Yoshie, 2020), arrays of mounted obstacles (Coceal et al., 2014; Fuka et al., 2018; Goulart et al., 2019), and urban canopies close to reality (Auguste et al., 2020; Hertwig et al., 2021). While for single buildings, the number of variables reduces to the shape and orientation of the obstacle relative to the approaching flow, the relative position of obstacles to each other (aligned vs. staggered) is at least as important for building arrays. In the aligned case, buildings may contribute to horizontal dispersion by channelling the mean flow through wind-parallel street-canyons, which can be further enhanced by isolated tall buildings (Fuka et al., 2018). On the other hand, transversal and vertical dispersion is more pronounced in the staggered case. For vertical dispersion, both the contributions by the mean flow from the diverging streamlines in front of the upstream faces and turbulent dispersion in the building wakes are of similar importance (Goulart et al., 2019). Buildings do not only enhance dispersion but can also trap pollution within horizontal re-circulation zones, which then act as secondary

https://doi.org/10.5194/gmd-2021-358
Preprint. Discussion started: 22 November 2021


Geoscientific Model Development Discussions
Open Access
EGU

sources (Coceal et al., 2014). Furthermore, while vertical transport in proximity to sources leads to an efficient detrainment of air pollution from near the surface, it may be re-introduced further downstream through down-washing processes, especially in the vicinity of tall buildings (Goulart et al., 2018). On a larger scale, the extraction of energy from the mean flow by buildings causes the roughness sublayer, within air pollution is efficiently mixed, to grow in thickness, an effect which is especially pronounced for a heterogeneous building-height distribution (Hertwig et al., 2021; Makedonas et al., 2021). Differential heating of opposing building walls, depending on the flow direction, enhances or hampers the development of the street-canyon vortex (Louka et al., 2002; Marucci and Carpentieri, 2019). Temperature differences may also occur between the roof level and the ground level and can have similar consequences (Park et al., 2016). On a larger scale, anthropogenic heating, radiation trapping and heat storage within building walls increases the magnitude of the urban-heat island effect (Kotthaus and Grimmond, 2014). The positive surface-sensible-heat flux destabilizes the urban planetary boundary layer (PBL), which in combination with wind shear from the mechanical building effects leads to an increase in PBL height (Roth, 2000).

Exposure studies depend on modeling of the various aspects in addition to point monitoring observations and, recently, also measurement networks. However, there remains a gap between the need for an accurate estimation of pollutant concentrations at various characteristically unique exposure sites across the urban scale and the limited applicability of consulted model data for this purpose. Mesoscale chemistry-transport models (CTMs) are used to simulate emission, regional transport, deposition and chemistry of a multitude of pollutant species (Wolke et al., 2012; Cames and Eckard, 2013). Therein, the effects of an urban canopy can be included by urban-canopy parameterizations (Martilli et al., 2002; Schubert et al., 2012). Nevertheless, the spatial resolution applied with such models is generally too coarse for a representation of the true magnitude of the intra-urban variability. Also, building effects at the microscale, like pollution trapping or horizontal channeling, cannot be considered in such a parameterized form. As a consequence, urban air pollution fields modeled with CTM's are typically representative to the urban background (Korhonen et al., 2019). Dealing with the necessity to more accurately represent the urban variability, but at the same time to avoid the prohibitively large computational costs of microscale model applications at the meter scale, we presented the urban dispersion model CAIRDIO with diffuse-obstacle boundaries in Weger et al. (2021a). Therein, we recognized the model scale gap between the mesoscale and the urban microscale, and the advantage of gray-zone horizontal resolutions between these two scales from a computational perspective. Model comparison with an idealized wind-tunnel experiment, also included in Weger et al. (2021a), showed that relevant aforementioned mechanical building effects can be represented to a satisfactory degree for valid dispersion simulations performed at horizontal gray-zone resolutions ($\Delta h = 40\,\mathrm{m}$). Most importantly, buildings influenced dispersion with the mean flow in a correct way most of the time, even when obstacles are described as diffuse features similar to a porous medium representation. Turbulent fluxes from buildings, on the other hand, are predominantly parameterized at such comparatively coarse resolutions, which makes model results sensitive to the prescribed mixing length.

In this follow-up paper we shift the focus from idealized experiments to a more application-oriented use of the model for a real city and true atmospheric conditions, for which the mid-sized city of Leipzig in Germany is selected as a showcase. This allows us to include further processes in the model, which are paramount for realistic dispersion simulations within a real urban canopy and realistic meteorology. For example, the stratification of the PBL does not necessarily have to be neutral and

https://doi.org/10.5194/gmd-2021-358
Preprint. Discussion started: 22 November 2021


Geoscientific Model Development Discussions

can be further modified locally in the model by a parameterized surface-heat flux from ground and building surfaces. Inflow conditions are in general not only turbulent but also transient, in order to account for an accurate evolution of the larger-scale meteorology. The complexity of the simulation is further increased by using a comprehensive emission inventory that includes all relevant sectors, which are modulated in time to account for diurnal and weekly changes in activity. While this study aims not at analyzing individual processes in depth, its main objectives are to demonstrate the feasibility and practicability of the approach as a downscaling tool for a more accurate representation of the intra-urban air-pollution variability. Therefore, apart from static inputs, the model solely relies on the output fields of a host simulation conducted at the lower end of the mesoscale, for which the CTM COSMO-MUSCAT (Wolke et al., 2012) is used. For validation, we compare modeled PM_{10} and/or BC concentrations with measurements at 5 different operational air-monitoring sites in Leipzig for a total period of two consecutive days in spring 2020. To further estimate the sensitivity to the horizontal resolution, locally-nested sensitivity runs are performed, for which the horizontal resolution is increased from a default $\Delta h = 40\,\mathrm{m}$ in steps down to $\Delta h = 5\,\mathrm{m}$, enabling conventional building-resolved simulations.

The paper is structured as follows: Section 2 describes the methodology, in which all the general and technical aspects of the simulations and measurements are described. This also includes a detailed description of the mesoscale coupling. Section 3 includes the presentation and discussion of model results, which is subdivided into a part describing the modeled PBL evolution, a model evaluation with concentration measurements, including a comparison with results from the CTM COSMO-MUSCAT, and the grid-size sensitivity study. Section 4 summarizes the main findings of the study and highlights the advantages but also limitations of the demonstrated approach and the study itself.

2 Methodology

2.1 Study time period

The model case study spans 2 consecutive days from 1 March 2020, 00:00 UTC to 3 March 2020, 00:00 UTC, to address the main objectives of this study. Yet, for a more significant model evaluation with observational data, a substantially longer simulation period needs to be simulated. While principally our approach is computationally much cheaper compared to a well-resolved urban microscale simulation, a compromise still had to be found, and we decided to invest computation resources in a spatially more comprehensive simulation that fits better the aspect of a model case study. The specific simulation period was selected based on suitable properties for an investigation of the intra-urban air-pollution variability. Firstly, quality-assured observational data from all operational air-monitoring sites in Leipzig are available during this period. Secondly, significant impacts of the world-wide spreading Covid-19 pandemic had still not reached the German public by early March 2020, as data from the Google mobility report show a significant decline starting after 10 March (Google-LLC, 2020; Forster et al., 2020). This provided confidence that the traffic emissions had not to be adjusted for a reduced mobility, which is a potential source of additional uncertainty. Thirdly and most importantly, the meteorological conditions were suitable to focus on local air pollution and PBL processes affecting it. The large-scale synoptic pattern during the simulation period from 1 to 3 March 2020 was dominated by a large and deep low-pressure system situated over northwestern Europe, from which two troughs

https://doi.org/10.5194/gmd-2021-358
Preprint. Discussion started: 22 November 2021

Geoscientific Model Development Discussions
Open Access
EGU

protruded southward and eventually moved across Germany (see Figure 1a-c). The associated unsettled weather conditions in Leipzig resulted in diverse PBL characteristics and effects on local air quality, which are interesting to study. Moreover the influence of low pressure favored low background near-surface PM_{10} concentrations over most of Germany, as suggested by results from an air-quality simulation for Europe depicted in Fig. 1d-f. According to this, highest PM_{10} concentrations apart from the well-known air-polluted regions, like the Po Valley, occurred over the eastern half of Europe. There were also periods before and after the actual simulation period, when the Siberian high pressure system extended westward and brought a polluted continental air mass to central Europe (not shown). During such periods with elevated background concentrations, the intra-urban air-pollution variability was quite insignificant and not worth to study.

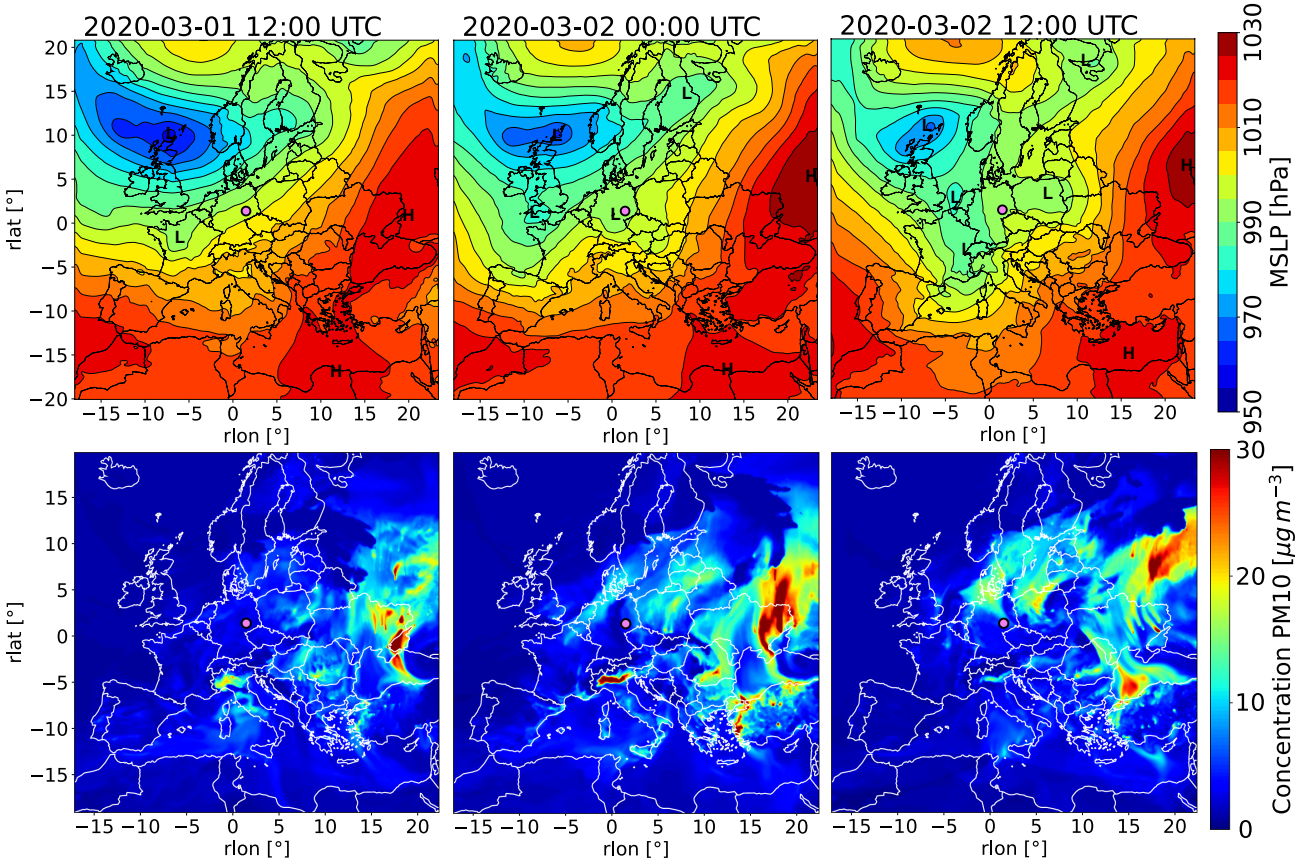

Figure 1. Overview of the synoptic-scale transport and air quality patterns over Europe during the simulation period in terms of maps of mean-sea level pressure (a-c), and modeled near-surface PM_{10} concentrations (d-f). The magenta dot marks the location of the city of Leipzig in eastern Germany. The maps are in rotated geographic coordinates, where the coordinates of the rotated pole are 40°N, -170°E.

https://doi.org/10.5194/gmd-2021-358
Preprint. Discussion started: 22 November 2021


Geoscientific Model Development Discussions
Open Access
EGU

2.2 Observations

For model evaluation a range of in-situ air quality observations is used. The south-eastern German state Saxony operates 26 air-quality monitoring sites. Three of them are suitable for our model evaluation, as they are located within the city margins of Leipzig and provide PM_{10} concentration measurements. One of the three stations considered is also co-operated by the TROPOS and provides BC retrievals too. Three stations are air quality stations operated by the Saxon State office while two additional stations belong to TROPOS. Three out of the five station measure also equivalent black carbon (eBC) mass concentration, which are also relevant to our evaluation. Tab. 1 lists some basic information of the aforementioned measurement sites, while Fig. 2 shows their locations on horizontal maps of the simulation domains to provide a qualitative overview of the characteristic environment, like the distribution of buildings, parks and major roads highlighted by PM_{10} line emissions. Finally, Fig. 3 gives a detailed mapping of the surrounding building environment in spherical coordinates at each exact measurement position, as well as the corresponding sky-view factors f_{sky}. Based on these information, a brief introduction of each measurement site is given in the following. Station Leipzig Lindenau (LL) measures PM_{10} and is located in the western city district Leipzig Lindenau within a closed street canyon running in WNW-ESE direction. The street canyon has average dimensions (height $\times$ width) of roughly $20\,\mathrm{m} \times 25\,\mathrm{m}$, which results in a sky-view factor of 0.34. The horizontal position of the measurement site is near the northern side of the canyon at a distance of only $5\,\mathrm{m}$ to a traffic-busy road (average daily traffic count (ADTC) of 20400 vehicles). This, in combination with an inlet height of $1.7\,\mathrm{m}$ leads to a high exposure of this station to the exhaust gases from nearby traffic, which clearly classifies this station as roadside / street canyon. Station Leipzig Mitte (Leipzig Center, LC) provides PM_{10} and eBC measurements. It is located southwest of the Leipzig main railway station at a junction of the inner-city ring, which is a multi-line road (ADTC of 47600 vehicles). Therefore, also this station is classified as roadside. Compared to the site LL, there is more open area around the station LC ($f_{sky} = 0.79$), with the closest significant building (height $times$ width of $27\,\mathrm{m} \times 50\,\mathrm{m}$) being to the south of the station at a distance of approximately $45\,\mathrm{m}$. Furthermore, due to a local park adjoining to the east, the influence of traffic emissions at the measurement site can be expected to vary according to the prevailing wind direction. Station Leipzig West (LW), located within the western outskirts of Leipzig inside a park, is a background station for PM_{10}, as it is also secluded by lines of trees from a nearby road (ADTC of 8600 vehicles). Station Leipzig Eisenbahnstr. (LE) has a long history as a scientific measurement site and is thus well documented from previous air-quality studies (see e.g. Klose et al. 2009, Wiesner et al. 2021). The measurement equipment is located next to a window on the third floor of an apartment house (inlet height is approx. $6\,\mathrm{m}$ above the road) flanking a frequently traffic-congested street canyon (ADTC of 11500 vehicles). The cross section of the street canyon is symmetric ($20\,\mathrm{m} \times 20\,\mathrm{m}$). Regularly occurring crossroads divide the street canyon into segments of $70\,\mathrm{m} - 110\,\mathrm{m}$ length, with the closest crossroad (ADTC of 11800 vehicles) being to the west at a horizontal distance of about $35\,\mathrm{m}$ from the measurement site. While this side is also classified as roadside, its inlet position high above the road makes it more representative to the average concentrations within the street canyon. Depending on the development of the street-canyon vortex, however, it may be also more directly exposed to high pollution concentrations. Finally, the side Leipzig TROPOS (LT) is a background station for eBC, as it is located on the roof top of the TROPOS institute's building at a height of $16\,\mathrm{m}$ and at a distance of at least $100\,\mathrm{m}$ from any busy roads.

https://doi.org/10.5194/gmd-2021-358
Preprint. Discussion started: 22 November 2021

Geoscientific Model Development Discussions

PM_{10} concentrations are directly and near-continuously measured using the tapered element oscillating microbalance (TEOM) system (scientific ambient particulate monitor TEOM 1405, Thermo Fisher Scientific Inc.). TEOM derives PM mass concentrations from the frequency-change of an oscillating hollow tube caused by deposited material at one end of the tube (Page et al., 2007). Real-time measurements are averaged to hourly-mean values with a stated precision of $\pm 2.0\,\mu g$ and an accuracy of $0.75\,\%$ (TFS, 2019). eBC is indirectly retrieved from optical principles with multi-angle absorption photometers (MAAP 5012, Thermo Fisher Scientific Inc.). MAAP estimated the absorption coefficient of an aerosol probe from the transmission and back-scattering of light at a wavelength of $637\,nm$, where eBC is the main absorber (Petzold and Schönlinner, 2004). The eBC mass concentrations calculated with a mass absorption cross section of $6.6\,m^2\,g^{-1}$ are assumed to be directly comparable with modeled BC mass concentrations, and have an uncertainty between 5 % and 12 % according to different sources (Wiesner et al., 2021).

Table 1. Overview of the air-monitoring sites used for model evaluation. For the pollutants, only the relevant species to our model evaluation are denoted. Note also, that the station Central is both a public and scientific site.

Label	**LL**	**LC**	**LW**	**LE**	**LT**
Location	Lützner Str.	Richard Wagner Str.	Schönauer Str.	Eisenbahnstraße	TROPOS building
Characteristics	street canyon W-E	multi-line road	park	street canyon W-E	roof top
Classification	roadside	roadside	urban background	roadside	urban background
Coordinates °E, °N	12.335, 51.336	12.377, 51.344	12.298, 51.318	12.401, 51.346	12.434, 51.353
Inlet height	1.7 m	4 m	4 m	6 m	16 m
Pollutants	PM_{10}	PM_{10}, BC	PM_{10}	BC	BC

2.3 Mesocale air-quality modeling

As air pollution is not only influenced by local processes, all relevant larger scale sources and transport have to be considered in the city-focused, urban microscale simulations in terms of boundary conditions. Such a multiscale approach requires tailored model setups with a scale-appropriate prioritization of the dominating processes. Besides the long-range transport, physico-chemical reactions contributing to significant secondary particulate matter (SPM) formation have to be considered on the continental and regional scales, for which in this study the online-coupled mesoscale CTM COSMO-MUSCAT (Wolke et al., 2012) is employed. Important multi-phase reactions leading to SPM involve the gaseous compounds ammonia, nitric acid, and sulfuric acid, which themselves are important air pollutants. Additionally, seasonally dependent secondary organic aerosol (SOA) formation is included in the set of chemical reactions composed by the mechanism RACM-MIM2 (Stockwell et al.,

https://doi.org/10.5194/gmd-2021-358
Preprint. Discussion started: 22 November 2021

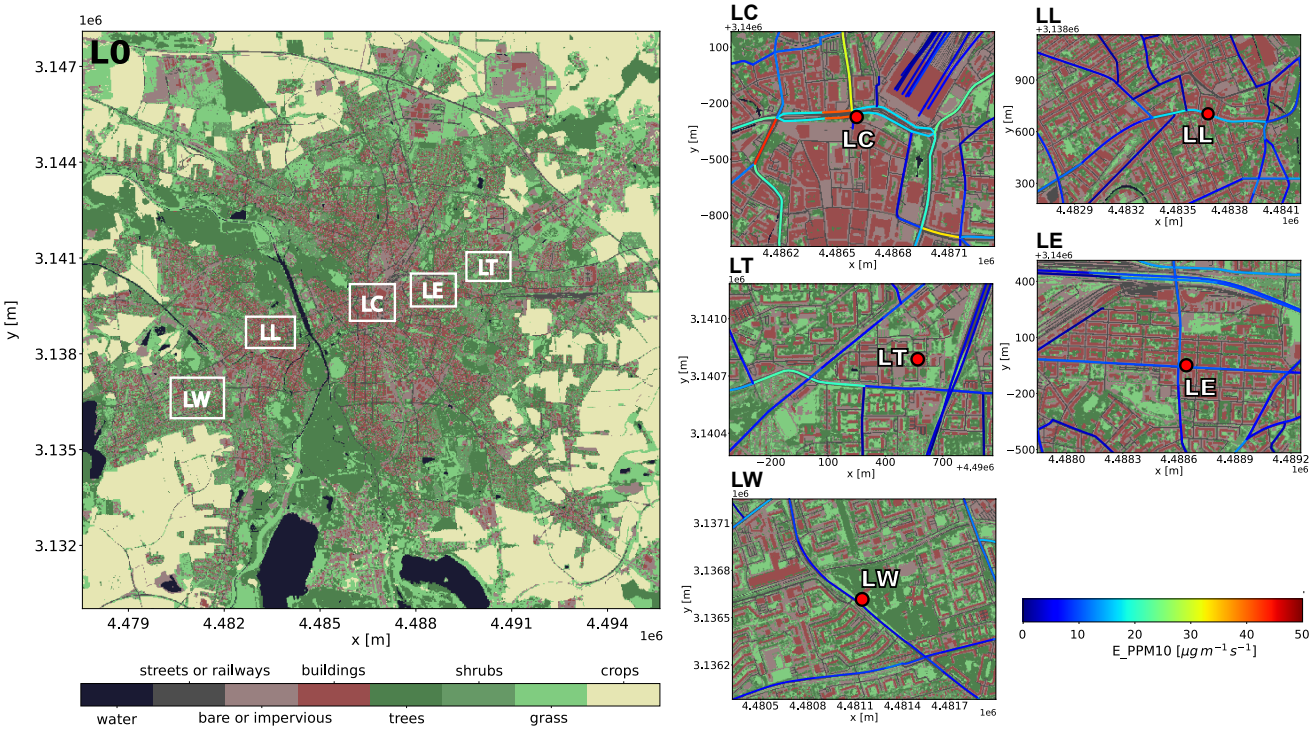

Figure 2. Map of the city area of Leipzig, which is also selected as the coarse-grid CAIRDIO simulation domain L0 introduced in Section 2.4.1. Each of the white boxes contains an operational air monitoring site used for model evaluation. In addition, a magnified view of the area within each box shows the local environment around the corresponding air-monitoring site, which is highlighted by a red circle. These areas also correspond to the CAIRDIO subdomains introduced in Section 2.5. Traffic-PPM$_{10}$ emissions of major roads are represented by line sources.

1997; Taraborrelli et al., 2009). The remaining fraction of PM$_{10}$ is primarily emitted (PPM), and approximated by chemically inert tracers that are only subjected to physical atmospheric removal processes. Figure 4 gives an overview of the bulk PM$_{10}$ decomposition in MUSCAT as it is available from the model output. COSMO-MUSCAT is applied on a hierarchy of refined domains, with a one-way nesting technique providing the boundary condition for each consecutive simulation (see Figure 5 for an overview of the domains). This model setup has already been used to provide quasi-operational air-quality forecasts for the citizen-science campaign WTImpact (Heinold et al., 2019; Tõnisson et al., 2021). The outermost domain M0 has a spatial resolution of $14\,\mathrm{km}$ and covers entire Europe. This domain is initialized and driven by meteorological data from the global model ICON (Zängl et al., 2015) operationally run by the German weather service (Deutscher Wetterdienst, DWD). Initialization and boundary condition for air chemistry are interpolated from operational air-quality forecasts with the model system ECMWF IFS (Copernicus Atmosphere Monitoring Service) (Flemming et al., 2014). The domain M0 is simulated for an extended period in time (at least two weeks) ahead of the actual simulation period of two days. This allows for a proper

https://doi.org/10.5194/gmd-2021-358
Preprint. Discussion started: 22 November 2021

Geoscientific Model Development
Discussions
Open Access
EGU

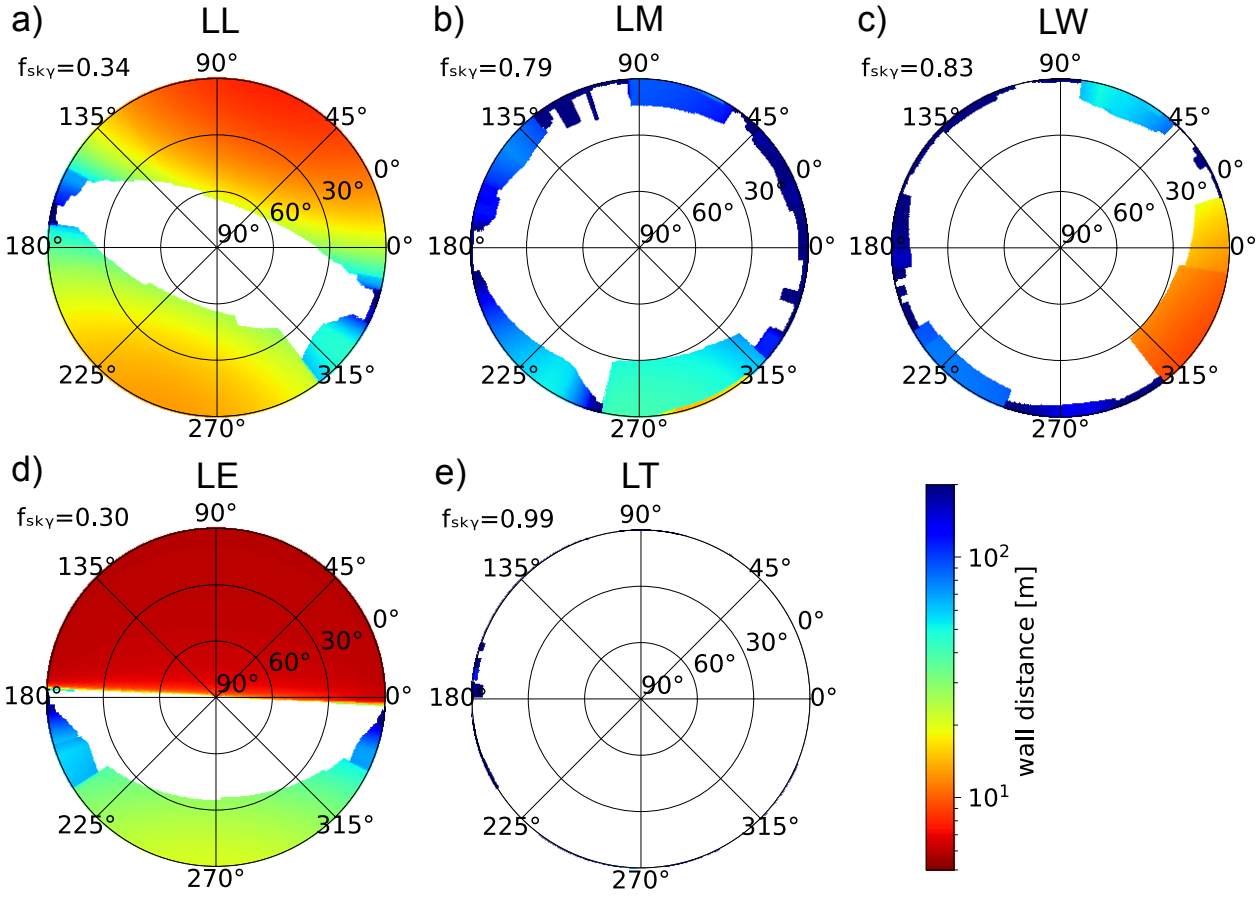

Figure 3. Simulated view on surrounding buildings in spherical coordinates at the exact 3-D locations of the inlets for the stations (a) LL, (b) LC, (c) LW, (d) LE, and (e) LT. The colors indicate the distance of instrument inlets to building walls, while visible sky is shaded in white. Additionally, the sky-view factors f_{sky} are computed as the fraction of the solid angle of the hemisphere not blocked by buildings.

relaxation of the initial distribution of air-chemistry constituents to the new model setup, as a different meteorological model, air-chemistry mechanism, and emission dataset are used. Simulation results for air chemistry are interpolated on domain M1 with $2.2\,\mathrm{km}$ resolution covering middle/eastern Germany, part of Czech Republic and Poland. For more accurate meteorological boundary conditions, re-analysis data from the operationally run COSMO-D2 model is used instead of the meterological output from domain M0. Output from domain M1 is interpolated on domain M2 with $1.1\,\mathrm{km}$ resolution. Simulation results from domain M2 are finally interpolated on the innermost domain M3 near the lower end of the mesoscale with $550\,\mathrm{m}$ horizontal resolution containing the city of Leipzig in its center. At this scale, the influence of the urban canopy and building environment is already considered based on the double-canyon effect parameterization (DCEP) by (Schubert et al., 2012). DCEP includes

https://doi.org/10.5194/gmd-2021-358
Preprint. Discussion started: 22 November 2021

Geoscientific Model Development Discussions

3 different types of urban canopy elements (ground, wall and roof elements), which are configured in idealized double canyon segments. A preprocessor is used to derive horizontal coverage of these segments in each grid cell, as well as probabilistic and geometric parameters of the canopy elements using a detailed building geometry dataset available for entire Saxony. DCEP computes surface fluxes for momentum, heat and turbulent kinetic energy (TKE), as well as solves the equations for radiative transfer and heat balance of the canopy elements. From the latter mean temperatures are available too.

The classification of emissions into various sectors is based on Selected Nomenclature for Air Pollution (SNAP). Emissions used for domain M0 are interepolated from the TNO-MACC2 dataset of the year 2009 (Kuenen et al., 2014). For the domains M1 and M2, German-wide emissions are provided by the German Environment Agency (Umweltbundesamt, UBA) for the year 2015, while emissions for the Czech Republic and Poland are again based on the aforementioned TNO-MACC2 emissions. The emission datasets for domain M3 and the consecutive CAIRDIO domains are primarily based on the emissions from UBA. However, the line emissions for traffic within the city margins of Leipzig are provided by Sächsische Landesamt für Landwirtschaft, Geologie und Umwelt (LfULG) for the year 2015 with greater spatial accuracy.

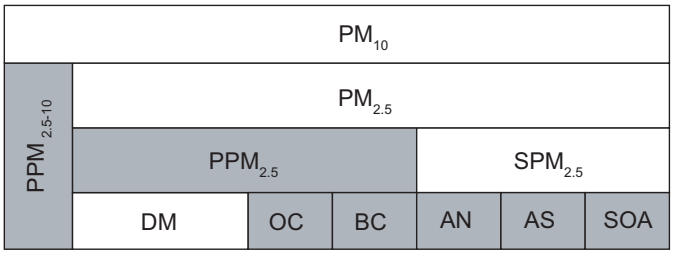

Figure 4. PM decomposition in the mesoscale CTM COSMO-MUSCAT: PM_{10} is the bulk mass concentration of all particles with mean diameter $d < 10\,\mu m$. PM_{10} is further composed into the two size fractions $PPM_{2.5-10}$ (primary matter) and $PM_{2.5}$. $PM_{2.5}$ again contains primary contributions from BC, organic carbon (OC), and dust and metallic particles (DM). The secondary fraction is mainly composed of ammonium nitrate (AN), ammonium sulfate (AS) and secondary-aerosol (SOA) particles. Boxes colored in gray indicate direct model outputs.

2.4 Intra-urban scale dispersion modeling

2.4.1 CAIRDIO domain L0

The intra-urban scale is addressed with the large-eddy simulation-based dispersion model CAIRDIO. This model includes an explicit representation of buildings by implementing diffuse obstacle boundaries (DOB), which work for a wide range of horizontal grid resolutions. These also include non-eddy-resolving resolutions where a large part of turbulent mixing is parameterized. For a detailed description of CAIRDIO v1.0, the reader is referred to Weger et al. (2021a). In appendix A improvements of the actually used model version v2.0 are listed. For the close-up city simulation, domain L0 is horizontally resolved with uniform $40\,m$ grid spacing. This resolution showed to be satisfactorily accurate in a first model validation study

https://doi.org/10.5194/gmd-2021-358
Preprint. Discussion started: 22 November 2021

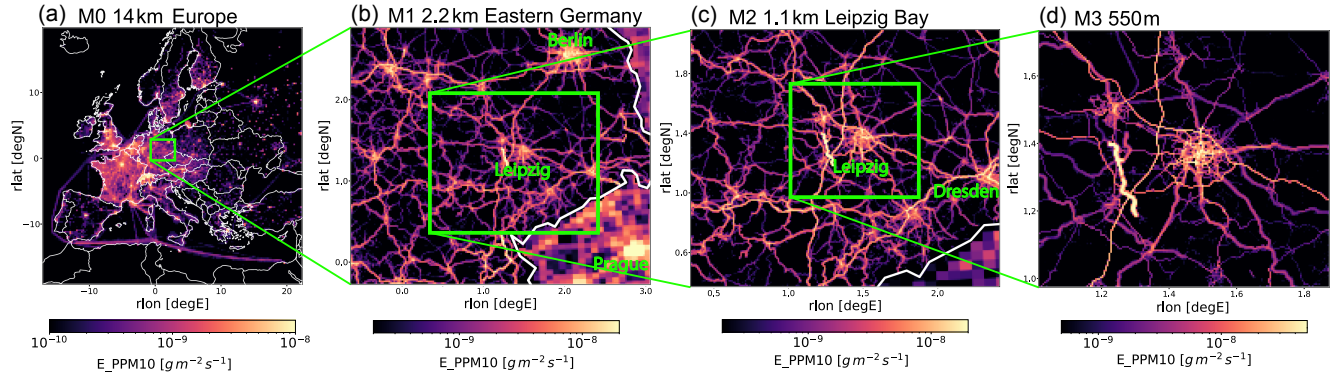

Figure 5. Nested domains of the precursor simulations using COSMO-MUSCAT: (a) M0, 14 km, (b) M1, 2.2 km, (c) M0, 1.1 km, and (d) M3, 550 m. Displayed are the primary PM_{10} emissions of the transport sector (SNAP categories 7 and 8). Note that the displayed range differs between the plots to account for the increased resolution of road emissions from (a) to (d). The maps are in rotated geographic coordinates, where the coordinates of the rotated pole are 40°N, -170°E.

based on wind-tunnel data also presented in Weger et al. (2021a). For DOB, the same geometric building dataset as already used for deriving the parameters in DCEP is used. At the horizontal scale of $40\,\mathrm{m}$, buildings are effectively represented as diffuse obstacles. As a consequence, the subgrid-scale mixing length is of similar magnitude or even larger than the average space between buildings. This implies that the simulation is mostly non-eddy resolving (similar to a RANS approach) within the urban canopy. For a more accurate representation of vertical gradients and mixing processes near the surface, the vertical dimension is kept much finer resolved, with $5\,\mathrm{m}$ grid spacing within the urban canopy. Increased grid stretching is applied above, with a maximum stretching factor of 4 near the domain top. Note that vertical resolution is not as computationally expensive as horizontal resolution, because the Courant-Friedrichs-Lewy (CFL) criterion, which limits the explicit integration time step, is mostly determined by the horizontal wind speed. The horizontal coverage of domain L0 is roughly $18\,\mathrm{km} \times 18\,\mathrm{km}$, which is extensive enough to not only accommodate the complete city of Leipzig but also a sufficient fetch to allow for a relaxation of the lateral boundary conditions. The domain top is located at about $350\,\mathrm{m}$ height, which is generally below the vertical extend of a typical convective PBL. However, a suitable boundary condition allows for vertical motions exiting/entering at the domain top, which is further explained in the subsequent paragraph 2.4.2 addressing the mesoscale forcing. While the surface orography within domain L0 is not mountainous, subtle effects from it can still influence meteorology. CAIRDIO can be used with terrain-following coordinates, which in this simulation are inferred from surface elevation data (DGM1) provided by the Staatsbetrieb für Geobasisinformation und Vermessung Sachsen (GeoSN). This dataset with a spatial resolution of $1\,\mathrm{m}$ has also been corrected for vegetation and buildings and is thus compatible with the explicit representation of buildings by DOB. Surfaces fluxes of momentum, heat and moisture from vegetation, as well as other types of land cover (lakes, bare soil, subgrid-scale structure of buildings) are parameterized using Monin–Obukhov similarity theory. Therein, each surface type is

https://doi.org/10.5194/gmd-2021-358
Preprint. Discussion started: 22 November 2021


Geoscientific Model Development Discussions
Open Access
EGU

characterized by a parametric roughness length z_0. Table 2 lists the z_0 values related to each land-cover class used in the model. Land-cover is based on a combination of the Pan-European land cover map for 2015 with $30\,\mathrm{m}$ spatial resolution (Pflugmacher et al., 2018), and the more detailed land-cover map by Banzhaf and Kollai (2018) (better than $5\,\mathrm{m}$ resolution) for most of the urban area. The combined dataset is depicted in Fig. 2 for domain L0, as well as for the finer resolved nested subdomains introduced in the paragraph 2.5 addressing the LES-to-LES nesting.

The emissions used for domain L0 are on the same basis as the ones already used for mesoscale domain M3, but are locally refined were applicable. Road and railway emissions (SNAP 7 and partly SNAP 8) are available as line sources and can in principle be gridded on arbitrary grids. In our setups, both the building geometries and line emissions are geometrically consistent to each other. Other sources from industry (SNAP 3, SNAP 4, SNAP 6, SNAP 9) and residential combustion (SNAP 2), as well as non-classified mobile sources (SNAP 8) are all originally given on a grid with $500\,\mathrm{m}$ spacing. Conveniently, the metadata of the building-geometry dataset provide additional purpose-based classification into residential and commercial buildings. This permits to relocate the corresponding area sources at the building roofs (whereas the building-volumes are taken as weights) and a subsequent gridding of the building emissions on the finer L0 grid. The advantage of this emission downscaling is currently investigated in a separate sensitivity study. The static emission fields are modulated with a time profile also taken from the TNO-MACC2 database. The spatially integrated and temporally modulated emissions are shown in Fig. 6. Accordingly, the traffic sector is by far the most important contributor to BC emissions during the simulation period.

Table 2. z_0 values of the different land-cover classes used in all CAIRDIO simulations.

Land-use class	z_0
Water surface	$0.001\,\mathrm{m}$
Bare soil	$0.01\,\mathrm{m}$
Grass land	$0.03\,\mathrm{m}$
Crop land	$0.07\,\mathrm{m}$
Shrubs	$0.3\,\mathrm{m}$
Trees	$1.0\,\mathrm{m}$
Streets and railways	$0.1\,\mathrm{m}$
Buildings	$0.2\,\mathrm{m}$
Other impervious surface	$0.05\,\mathrm{m}$

https://doi.org/10.5194/gmd-2021-358
Preprint. Discussion started: 22 November 2021

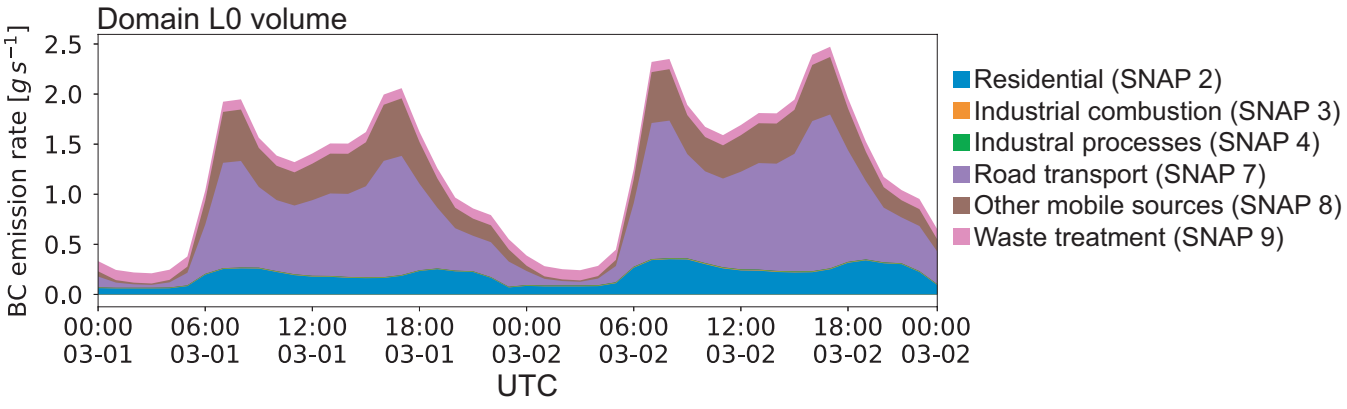

Figure 6. BC emission rate (TNO-MACC2 time profile) vs. simulation time for the complete domain L0 subdivided into the relevant SNAP categories.

2.4.2 Mesoscale forcings and boundary conditions

Simulation results from COSMO-MUSCAT mesoscale domain M3 are used to drive the meteorological and air-pollution fields of the city-scale domain L0. Initial and boundary conditions for the meteorological prognostic fields, which include the 3-D wind components, potential temperature Θ, specific humidity Q_v, and subgrid-scale TKE E_{sgs}, are spatially interpolated using tricubic interpolation. For the air-pollution fields instead, trilinier interpolation is used. The 3-D interpolation procedure is carried out as a sequence of 2-D horizontal interpolation followed by vertical interpolation. For the horizontal interpolation, the Climate Data Operators (CDO) software (Schulzweida, 2019) is used, which is convenient to remap data from rotated lat/lon coordinates of the COSMO-MUSCAT model directly to Lambertian azimuthal equal-area coordinates (epsg:3035) of the L0 grid. Vertical interpolation is based on the 3-D height of half levels (HHL), which coincide with the locations of vertical velocity of the staggered grid. After horizontal remapping of the HHL field of the M3 grid, the vertical interpolation weights are generated by computing Lagrange polynomials of the desired accuracy from the HHL data. As the CAIRDIO simulation employs a finer grid spacing near the ground than COSMO-MUSCAT, the first vertical levels need to be extrapolated, for which a level with zero-height is introduced. At this zero-height level, all wind components are set to zero, and the potential temperature as well as specific humidity fields assume the respective surface values Θ^S and Q_v^S. For the air-pollution fields, constant values from the first MUSCAT layer are extrapolated.

Lateral boundary conditions for the prognostic subgrid-scale TKE equation in the microscale model CAIRDIO are derived by applying a scale separation to the spatially interpolated subgrid-scale TKE of the COSMO-MUSCAT simulation (denoted by coarse) E^c_{sgs}. E^c_{sgs} is split into a part E^f_{res} that can be resolved on the CAIRDIO L0 grid (denoted by fine) and a still unresolvable component E^f_{sgs}. The energy splitting can be approximated by integrating the well-known Kolmogorov spectrum

https://doi.org/10.5194/gmd-2021-358
Preprint. Discussion started: 22 November 2021


Geoscientific Model Development Discussions

for the inertial subrange $E(k) \propto k^{-5/3}$ up to the different cut-off wave-numbers k_{min} of the fine and coarse grids. k_{min} can be directly related to the subgrid-mixing scale Δ_{sgs}, then the following expression follows:

$$E^f_{sgs} = E^c_{sgs} \left(\frac{\Delta^f_{sgs}}{\Delta^c_{sgs}} \right)^{2/3} . \tag{1}$$

Δ^f_{sgs} can be crudely approximated by twice the horizontal grid spacing (corresponding to the Nyquist wavenumber). Note that the horizontal grid spacing in typical PBL simulations is equal or larger than the vertical grid spacing and is thus the dominant cut-off scale. Δ^c_{sgs}, on the other hand, can be related to the master-mixing length of the mesoscale simulation. E^f_{sgs} is finally the lateral boundary condition for the prognostic subgrid-scale TKE equation, which determines the eddy diffusivities. The lateral boundary condition for the 3-D wind vector is a Dirichlet/radiation condition that can flexibly distinguish inflow from outflow regions. For inflow regions, a superposition of the interpolated mesoscale wind field and recycled turbulence is prescribed. The scale-separation applies in a similar way for the turbulence recycling scheme, as the cut-off wavelength of the extraction filter is chosen similar to Δ^c_{sgs}. Consequently, the recycled turbulent fluctuations are scaled with the resolvable energy part E^f_{rec}. Convective PBLs that cannot be simulated for their entire vertical extend require a boundary condition that allows for turbulent motions transcending the top-domain boundary, while the mesoscale forcing shall still apply at the same time. A mixed Dirichlet/Neumann condition addressing both scale ranges independently in principle can satisfy these requirements. In practical simulations, however, the small-scale fluctuating Neumann contribution eventually tended to grow exponentially, which required a rescaling with E^f_{rec} and a limiting of the maximum amplitude of vertical motions for numerical stabilization.

Besides the initial and boundary conditions for the prognostic fields, another important mesoscale forcing includes the coupling with the land surface, as surface potential temperature Θ^S and surface specific humidity Q^S_v are not computed in CAIRDIO. In this study, a land-cover based fitting method is favored over a more simple polynomial interpolation of the corresponding mesoscale surface fields. In doing so, much of the spatial detail can be preserved by assuming that land-cover is the most significant co-determinant of the small scale variability. This may only be valid for small horizontal domain extents and may require the application of an additional bilinear, or higher-order correction if more significant large-scale variations are present. In the following, the unknown potential temperature fluctuations ${\Theta^{S\prime}}_{Lc}$ of each considered land-cover class from a spatially filtered state $\overline{\Theta}^S$ are obtained by solving a least-square problem using the mesoscale data fields from the COSMO model:

$$||\mathbf{L}{\Theta^{S\prime}}_{Lc} + b - \Theta^{S\prime}|| =! min, \tag{2}$$

with $\Theta^{S\prime} = \Theta^S - \overline{\Theta}^S$. Note that the large scale variations not related to different land-cover classes have to be excluded in $\Theta^{S\prime}$ at this point. The matrix $\mathbf{L}$ is of shape $m \times n$, and contains the fractional land cover f_{Lc} for the total number of land-cover classes m with unknown potential temperature and number of grid cells n of domain M3. The vector b contains the potential temperature contribution from a-priori determined land-cover classes. A simplification leading to more robust fitting results considers only forests, open vegetation (grass, shrubs, crops) and bare soil (not including impervious urban surfaces)

https://doi.org/10.5194/gmd-2021-358
Preprint. Discussion started: 22 November 2021

Geoscientific Model Development Discussions

as independent classes. Already determined are the surface temperature and specific humidity values of water surfaces, as these values are spatially constant in the mesoscale simulation. Additionally, the urban parameterization DCEP in COSMO provides potential temperature estimates for impervious ground surfaces and roof surfaces at building sites, which both are included in b. After solving Eq. 2, the obtained land-cover dependent fluctuations ${\Theta^S}'_{Lc}$ are added to the interpolated filtered state $\overline{\Theta}^S$ to compose the new surface potential temperature field on domain L0 using the much higher resolved land-cover data. Because CAIRDIO uses a 3-D building structure, potential temperature values from these elevated horizontal and vertical surfaces are still missing. These values can, however, directly be interpolated from the additional output fields of the mean roof and wall temperature computed with the DCEP parameterization. Q_V^S is fitted in a similar fashion to Θ^S, with a further simplification that Q_V^S is set to zero for the impervious surface fraction. Thus, rain evaporation is neglected. Fig. 7 demonstrates the described downscaling approach based on an exemplary Θ^S field for 2 March 2020, 12 : 00 UTC, when sunshine prevailed. For the resulting reconstructed field of domain L0, a top-down projection is shown. The sun-lit roofs are the warmest surfaces with quite a spatially uniform distribution due to a constant prescribed roof albedo of 0.16 in DCEP. Considerably cooler are the ground surfaces inside the partly shaded street canyons, followed by the forest areas, and finally by the seasonally cold lakes with the lowest surface potential temperature. While in the given example, surface orography is mostly flat and the surface elevation could be neglected as an additional disturbing factor, this approach may be an oversimplification for areas with more mountainous terrain.

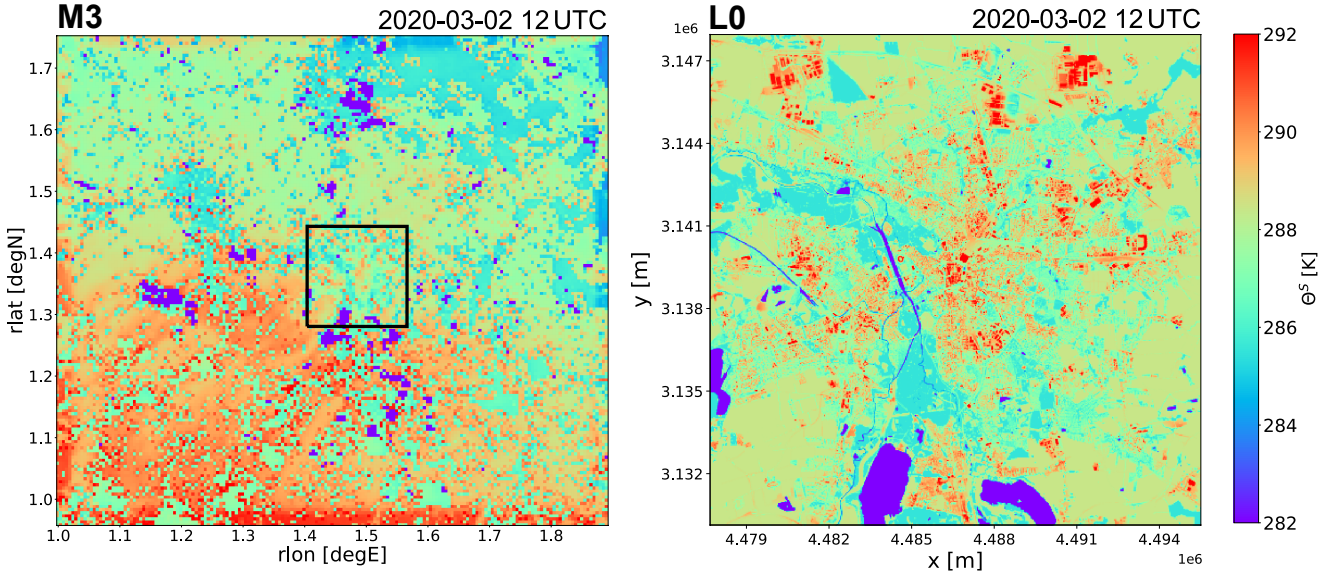

Figure 7. Diagnostic Θ^S downscaling from the mesoscale COSMO-MUSCAT domain M3 to the urban-microscale CAIRDIO domain L0 as by the explained land-cover method in Sect. 2.4.2.

https://doi.org/10.5194/gmd-2021-358
Preprint. Discussion started: 22 November 2021


Geoscientific Model Development Discussions

2.5 One-way LES to LES nesting

In order to quantify the influence of spatial resolution on results of the city-scale CAIRDIO simulations, spatially limited sub-domains LW, LL, LC, LE, and LT, each of them centered around an air monitoring site, are offline-nested into the parent domain L0. For these local domains, the horizontal grid spacing is gradually decreased from $40\,\mathrm{m}$ to $5\,\mathrm{m}$. The finest grid spacing permits conventional building-resolved simulations. To drive such nested simulations, prognostic fields from the CAIRDIO domain L0 available in $30\,\mathrm{s}$ intervals are used. The horizontal interpolated is carried out in the same way as already explained for the mesoscale forcing fields in paragraph 2.4.2. Since both the parent and nested domains use the same vertical grid, vertical interpolation is not needed in this case. The lateral boundary conditions for the subgrid-scale TKE equation are again based on a scale splitting according to Eq. 1. Therefore now the coarse-grid subgrid-scale energy from the CAIRDIO L0 grid is used. For the resolved part E^f_{res}, which scales the inserted turbulent fluctuations at the inflow boundaries, a slightly modified formula is used in order to consider the missing contribution of numerical diffusion in E^c_{sgs}:

$$E^f_{res} = E^c_{sgs}\left[\left(\frac{\lambda_{cut}}{\Delta^c_{sgs}}\right)^{2/3} - \left(\frac{\Delta^f_{sgs}}{\Delta^c_{sgs}}\right)^{2/3},\right] \tag{3}$$

where the extraction-filter width is set to $\lambda_{cut} = 140\mathrm{m}$, which is considerably larger than $\Delta^c_{sgs} = 80\,\mathrm{m}$. Note that the use of an exponential filter function results in a smooth cut-off range, with λ_{cut} defined as the wavelength that is scaled e^{-1}-fold.
In Figure 8 the described nesting method with the energy-scale separation is demonstrated by an example with domain LE and $5\,\mathrm{m}$ spatial resolution, which features a stably-stratified, shear-driven PBL. The plots of the dominant velocity component v (Fig. 8a and b) show that well-developed turbulence already exists near the southern inflow boundary, which qualitatively matches the turbulence more distant from the boundary well. This is also quantitatively shown by the derived energy spectra shown for the x-dimension (Fig. 8c), which do not evolve much when moving further away from the inflow boundary. Note that the inertial subrange is followed by the dissipation range, which can be attributed to the combined (dissipative and dispersive) numerical error of the advection scheme at significant convective speeds (Yalla et al., 2021).
The surface fields Θ^S and Q^S_v are again obtained from the corresponding mesoscale fields using the land-cover based method described in Sect. 2.4.2. An additional scaling is applied, such that the computed horizontally averaged values are independent of the spatial resolution and also correspond to the average values of the congruent part of the parent domain.

3 Results

3.1 Synoptic and urban planetary-boundary layer meteorology

In the following, an overview of the meteorological conditions and resulting PBL characteristics during the simulation period from 1 March 2020, 00:00 UTC to 3 March 2020, 00:00 UTC is given. The implications of the variable PBL structure on the modeled concentrations and transport of local air pollution are then qualitatively discussed based on model outputs from the CAIRDIO domain L0. As already briefly mentioned in Section 2, the weather in Leipzig during the simulation period was

https://doi.org/10.5194/gmd-2021-358
Preprint. Discussion started: 22 November 2021

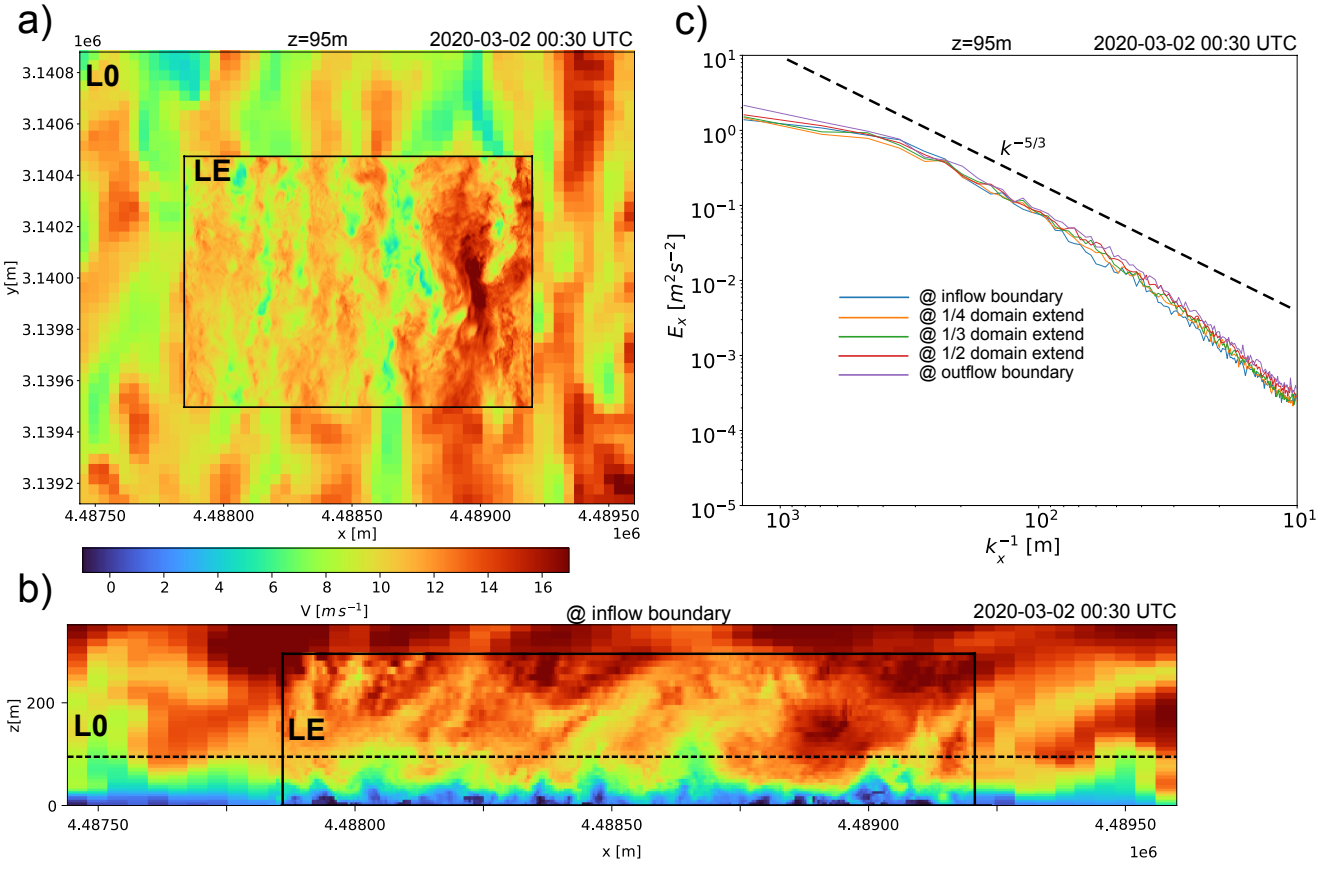

Figure 8. Depiction of a turbulent PBL flow simulated with the parent CAIRDIO domain L0 (40 m) and the offline-nested sub-domain LE (5 m) with a southern inflow boundary. In panel (a) the velocity component v is shown at 95 m height. Small-scale turbulence extracted from domain LE is superimposed on the interpolated coarse-grid wind field at the boundary-ghost cells, resulting in well-resolved turbulent structures at the inflow boundary as shown in (b) for the vertical plane. The horizontal dashed line in (b) marks the position of the horizontal plane shown in (a). In (c), spectra of resolved turbulent kinetic energy are shown for the x-axis at 95 m height and 5m horizontal resolution. Plotted are, the energy spectra at various positions along the y-axis.

influenced by low pressure. The large pressure gradients ahead of the troughs (see again Fig. 1a-c) imply windy conditions over Leipzig for most of the time as shown in Fig. 9a by the plotted wind barbs at 360 m height, which is at the top of domain L0. During the first simulation day, modeled wind speeds from the southwest reached up to 65 km h^{-1} in front of a first trough. During the consecutive day, winds were significantly weaker and varied more in direction during the passage of the aforementioned trough. The windy conditions were accompanied by a generally unsettled weather with a variable cloud cover on the first simulation day, and overcast skies intermitted only by a yet significant sunshine period around midday on 2 March. Small amounts of rain fell during the night from 1 to 2 March and at the end of the simulation period on late 2

https://doi.org/10.5194/gmd-2021-358
Preprint. Discussion started: 22 November 2021

Geoscientific Model Development Discussions

March, with amounts totaling $3\,\mathrm{mm}$ (Fig. 9b). The Θ_v-profile in Fig. 9c indicates different influences on the PBL stratification. Intermittent cloudiness during nighttime allowed for limited surface radiative cooling, while during the sunny periods surface heating caused the Θ_v gradient to diminish as the result of convective conditions. Striking is the warm-air advection just before the trough axes crossed the area (around 2 March, 00:00 UTC, and after the end of the simulation), which resulted in a large Θ_v-gradient within the lowermost $300\,\mathrm{m}$. The combined influences of vertical wind shear and stratification caused diverse turbulent conditions and considerable height variations of the mixed layer, as indicated by the gradient Richardson number (Ri) in Fig. 9d. During the first night, strong wind shear combined with an only weakly stable stratification resulted in a turbulent PBL with a mixing-layer height of about $400\,\mathrm{m}$. Conditions were also quite similar during 2 March from 00:00 UTC to 00:06 UTC. Nocturnal periods of warm-air advection significantly lowered the mixing-layer height to about $100\,\mathrm{m}$ or even below. In contrast, periods with strong solar irradiation resulted in convective conditions ($R_i < 0$), with a more significant event during the cloud-free period on 2 March around 12:00 UTC. While in the mesoscale simulation M3, PBL turbulence is generally unresolved, the most energetic eddies can be resolved outside the urban canopy with the $40\,\mathrm{m}$ grid spacing of domain L0. This is indicated by the vertical distribution of grid-scale and subgrid-scale TKE in Figure 10. However, from 2 March, 18:00 UTC to 23:00 UTC, and near the end of the simulation period, PBL turbulence was very weak or absent in the model as a result of the stable stratification.

In Figure 11, qualitative model results for two contrasting PBL states are featured as simulated with the CAIRDIO domain L0. In the first case (Fig. 11a), the dominant horizontal wind component v near the surface is shown for the stably-stratified, shear-driven PBL on 2 March at 00:30 UTC. Turbulence is organized into horizontal streaks near the surface as it is typical for a shear-driven PBL. The effect of significant surface roughness from the city structure and forest patches locally reduced the wind speed. Over these areas, turbulence was also of more intermittent nature due to the reduced vertical wind shear near the surface and limited turbulent energy production. The largest buildings, e.g., from factories can already be resolved with $40\,\mathrm{m}$ resolution, while the model representation of the air flow through the diffuse city structure consisting of smaller building units is more typical of a porous-media flow (see corresponding insets). Clearly, building-induced turbulence within the diffuse urban canopy cannot be resolved using such a still comparatively coarse grid spacing, but its mixing effects are represented by diffusion from the subgrid-scale model. The second case (Fig. 11b) features a convective PBL during midday of 2 March, which is induced by the positive surface-heat flux in the model. As a result of the calm wind conditions, convection organized into open cellular structures as depicted by vertical wind speed. These structures were more prominent over the extensive crop lands surrounding the city than within the city, where they were disrupted by the effects of buildings. Striking is also the absence of convection over the still cool lakes during this time of the year. The contrasting PBL properties between these two cases manifest themselves in the transport of locally emitted air pollution near the surface, as shown by the horizontal maps of BC concentrations in Fig. 11(c-d). In the case of the stably-stratified PBL, transport and mixing is mostly horizontal and as a result, locally concentrated sources, like from industry, generate long down-wind tails of elevated BC concentrations. Also modeled BC background concentrations in the stable case are relatively high ($0.3 \mu g\, m^{-3}$) compared to the convective case ($0.1 \mu g\, m^{-3}$), when the pollution is effectively diluted within a much deeper mixed layer. In the convective case, the rapid vertical mixing also limits the extend of horizontal dispersion from local sources. The resulting sharp horizontal gradients lead

https://doi.org/10.5194/gmd-2021-358
Preprint. Discussion started: 22 November 2021


Geoscientific Model Development Discussions

to a clearly visible imprint of the traffic network in the horizontal map of BC concentration, which dominated the emissions during this time. To support this qualitative discussion, the domain-averaged vertical turbulent flux of scalar BC is shown for both cases in Figure 12. In the stably-stratified case, vertical mixing is limited near the surface and only gradually increases with height. In contrast, the vertical flux in the convective case already peaks close to the surface and then gradually decreases with increased height, indicating an efficient lifting of the near-surface air pollution. Also in the convective case, the flux is much larger compared to the stable case, partly also due to the higher traffic emissions during daytime. Lastly, the partitioning into the resolved and parameterized fluxes shows that while the resolved flux is always dominant outside the urban canopy (the first $30\,\mathrm{m}$), the subgrid-scale flux has also a significant contribution, mainly close to the surface and in the stable case. This also indicates a significant model sensitivity to the mixing parameterization (e.g., the prescription of the static mixing length).

3.2 Quantitative model comparison with air-monitoring measurements

To quantitatively evaluate the model representation of the intra-urban variability of air pollution, hourly averaged model output of PM_{10} and BC concentrations are compared to respective measurements at the different air-monitoring sites within the city area of Leipzig. In addition, model output from mesoscale simulation M3 with $550\,\mathrm{m}$ horizontal resolution is added to the comparison to better quantify the benefit of the dynamic downscaling with $40\,\mathrm{m}$ horizontal resolution and explicit building representation with the CAIRDIO L0 domain.

In Figure 13, respective plots are shown for all monitoring sites in Leipzig (see details in Sect. 2.2). For the background station LT (Fig. 13a), the measured BC profile shows a clear diurnal cycle, with the lowest concentrations of about $0.1\,\mu\mathrm{g\,m^{-3}}$ during the morning hours of 1 March and 2 March around 06:00 UTC. Concentrations consistently peaked around 18:00 UTC on both days, which can be explained by the coincidence of high traffic emissions related to the rush-hour (see e.g., prescribed emission profile in Fig. 6) and a more shallow stably-stratified PBL during this time (see again Fig. 9e). In this respect, the morning peak on 2 March was damped by the increased PBL mixing height. On the morning of 1 March, which was a Sunday, no peak occurred at all due to the negligible traffic emissions at this time. Both the profiles from the mesoscale CTM and CAIRDIO simulations followed this observed evolution remarkably well. In the temporal mean, however, the COSMO-MUSCAT simulation tend to underestimate background BC concentrations based on the fractional bias (FB) $= 0.28$, which is improved in the CAIRDIO simulation to FB $= 0.07$. Nevertheless, the reasonably accurate model results can be considered as a good basis for the following discussion of the roadside stations LE and LC shown in Fig. 13b-c.

Compared to the background profile, the diurnal peaks are much more pronounced at the street-canyon site LE, with peak concentrations reaching up to $2.3\,\mu\mathrm{g\,m^{-3}}$ at 18:00 UTC on both days. The morning peak on 2 March is again much lower compared to the evening peaks, and night-time concentrations largely correspond to the observed urban background. For the site LC, which is situated in a more open environment, peak concentrations are expectedly lower compared to the site LE, or not pronounced at all. This can be most likely explained by the variable influence of the nearby traffic emissions depending on the prevailing wind direction. At both sites, the mesoscale simulation largely fails to capture the concentration peaks related to the nearby traffic emissions, as it essentially reproduces the same background profile depicted in Fig. 13a. As a consequence, a large positive bias results at both stations (FB $= 0.70 - 0.90$). In contrast to the mesoscale simulation, the CAIRDIO $40\,\mathrm{m}$ simulation

https://doi.org/10.5194/gmd-2021-358
Preprint. Discussion started: 22 November 2021

Geoscientific Model Development Discussions

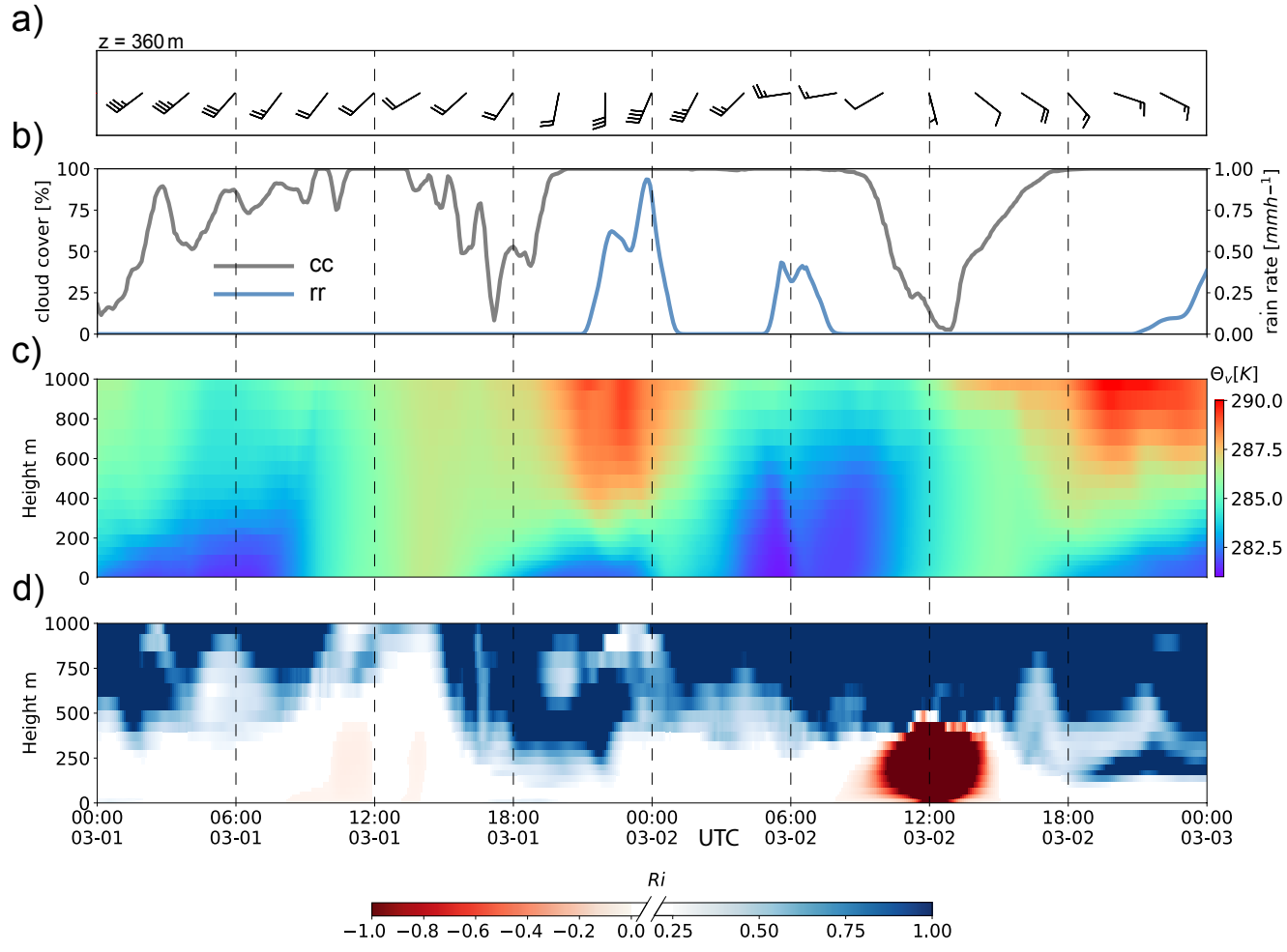

Figure 9. Overview of some horizontally averaged meteorological variables from simulation domain M3 influencing or being characteristic of the PBL structure. Shown are, (a) wind barbs within the lower free troposphere (1 km height), (b) cloud cover and rain rate, (c) virtual potential temperature Θ_v, and (d) the PBL stratification based on the bulk-Richardson number R_i.

shows a much more realistic profile at the site LE, which is clearly distinct from the background profile. While the observed evening peaks are still underrepresented, the morning peak and the elevated concentrations throughout the day of March 2 are modeled remarkably accurate. Also the gradual decline of concentrations during the night hours of early 2 March follows the observed profile very well. During the morning hours of 1 March, however, modeled concentrations are too high, which can be most likely attributed to the too high prescribed emissions. As a result of the stated improvements, the bias to measurements is reduced to FB $= 0.24$ in the CAIRDIO simulation at this site. For the site LC, the CAIRDIO simulation seems to better catch

https://doi.org/10.5194/gmd-2021-358
Preprint. Discussion started: 22 November 2021

Geoscientific Model Development Discussions
Open Access
EGU

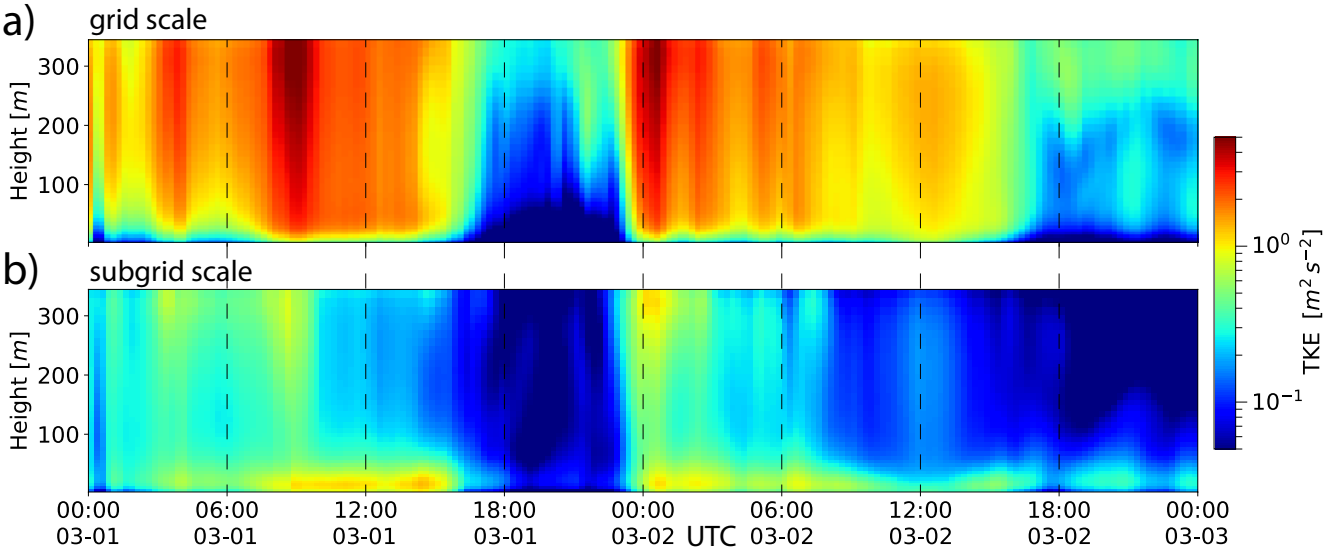

Figure 10. Horizontally averaged vertical distribution of grid-scale and sgs TKE versus time for simulation L0.

up to the measured peak concentrations, which is especially the case for the first observed evening peak. On the other hand, there are also concentration peaks apparent in the simulation that were not observed (e.g. morning peak on 1 March, evening peak on 2 March). The false peaks result in a moderately negative bias of the CAIRDIO model time series in reference to the measurements (FB $= -0.25$). While the discussed pollutant BC largely behaves like a passive scalar only subjected to physical deposition, the subsequent analysis of pollutant PM_{10} incorporates a much larger pool of model uncertainties related to the more diverse sources and also complex precursor chemistry of secondary aerosol. In this regard, it is not surprising to observe an already larger model uncertainty for the background profile at the site LW (Fig. 13d). While the measured profile shows only a small diurnal variability with significant noise superimposed on, the modeled profiles show more qualitative similarities with the modeled BC profiles as with the observations (i.e. smooth profiles with a significant diurnal cycle consisting of flat peaks around 18:00 UTC on both days). The reason for the observed short-term noise in the measurements may result from unknown local sources not represented in any of the models used. Model biases of both the mesoscale and CAIRDIO simulations are negative (-0.32 and -0.38, respectively), indicative of an overestimation of PM_{10} concentrations in the temporal mean. The measured PM_{10} time series at the street-canyon site LL (Fig. 13e) exhibits a significant diurnal variability. Again, the peaks at 18:00 UTC are suggestive of a significant influence of nearby traffic emissions. In fact, the profile shares, apart from the aforementioned noise, many characteristics with the measured BC profile at site LE. Not unexpectedly, the mesoscale simulation shows again little difference to the modeled background profile, which results in a significant positive model bias (FB $= 0.50$) at this site. A large improvement can be again observed when switching to the CAIRDIO simulation, which captured the diurnal variability of roadside PM_{10} concentrations very well. Only the maximum peak values during the first

https://doi.org/10.5194/gmd-2021-358
Preprint. Discussion started: 22 November 2021

Geoscientific Model Development Discussions

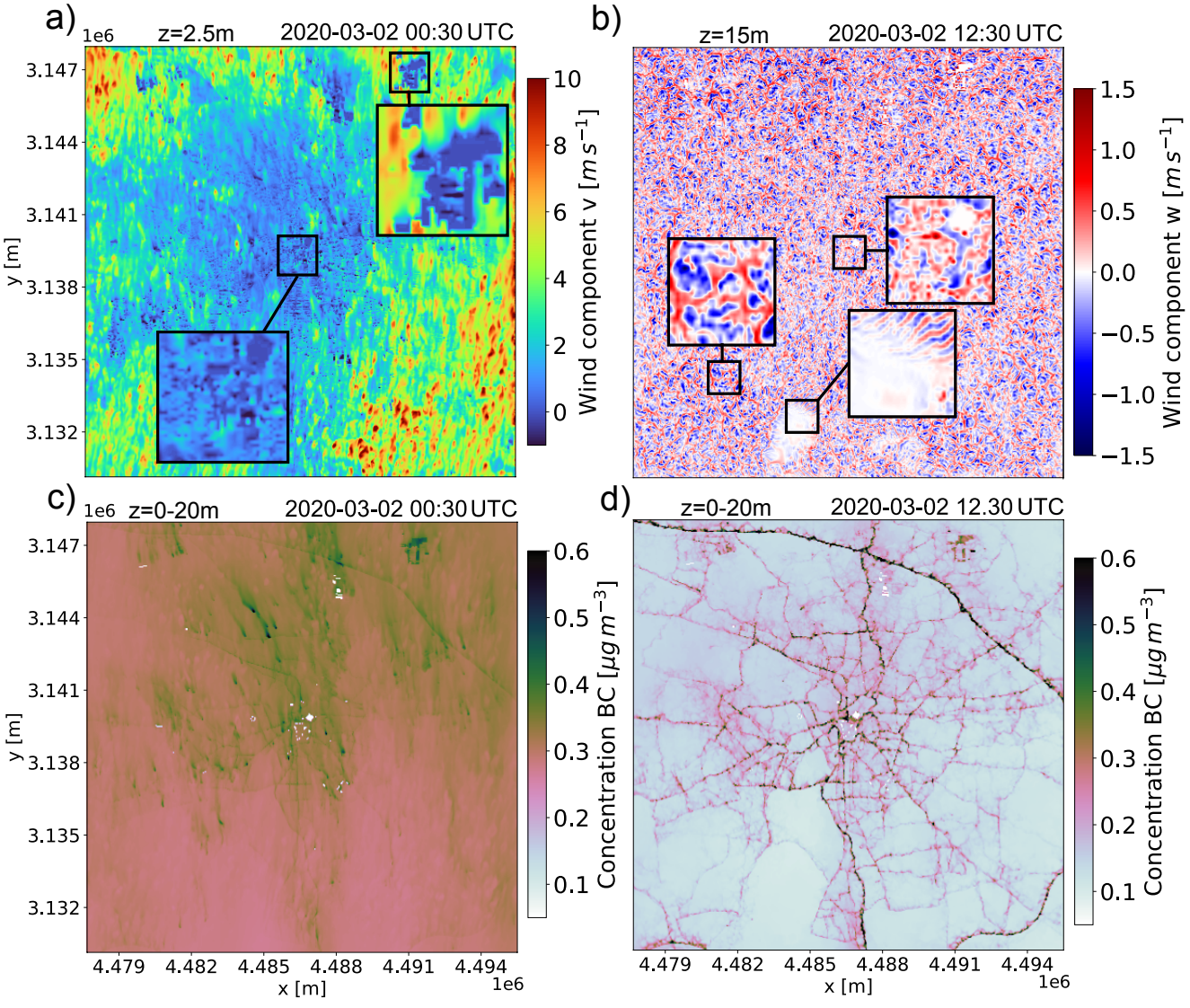

Figure 11. Horizontal map plots of simulation results with domain L0 (40 m) for two contrasting PBL cases: (a) shows the near-surface wind component v for a stably-stratified PBl, (b) the vertical component w for a convective PBL. The insets show a local magnification of some interesting flow features. In (c) and (d), the corresponding concentration fields for BC averaged within the height range 0 m-20 m are shown.

evening are underestimated. Correspondingly, the model bias is only slightly positive (FB $= 0.14$). Finally, the measured PM_{10} profile at site LC (Fig. 13f) is more comparable to the measured background at site LW, which is a bit surprising given that the station is classified as roadside. In anyway, measured PM_{10} concentrations seem to be more influenced by other not well-known sources than road traffic, at least for the investigated time period. As a result both models have their difficulties in representing

https://doi.org/10.5194/gmd-2021-358
Preprint. Discussion started: 22 November 2021

Geoscientific Model Development Discussions
Open Access
EGU

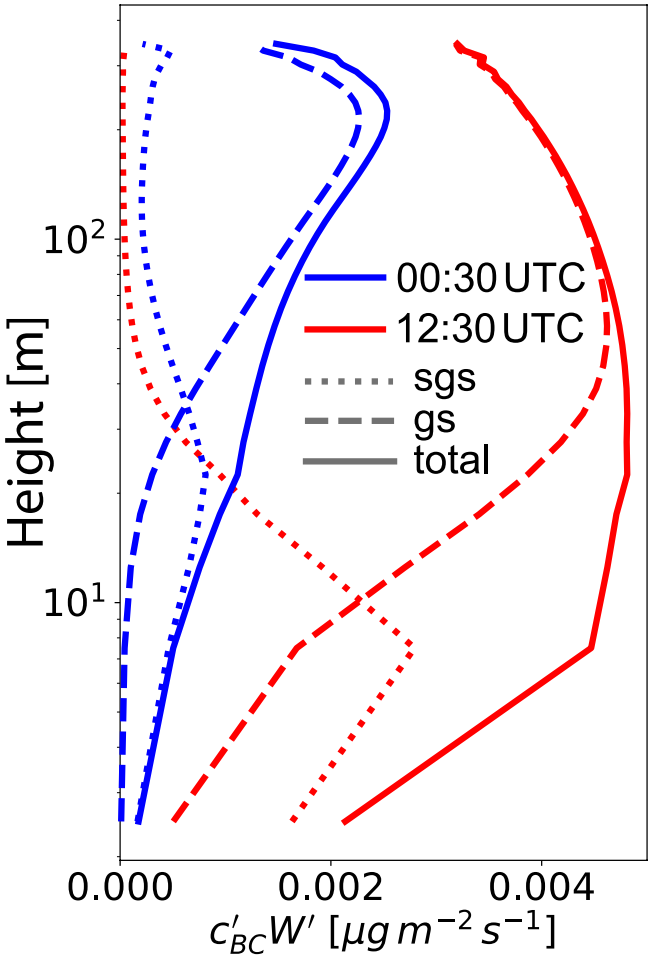

Figure 12. Vertical mixing of scalar BC within the PBL as simulated with CAIRDIO L0 on 2 March at 00:30 UTC featuring a stably-stratified PBL (blue lines) and on 2 March at 12:30 UTC featuring a convective PBL (red lines). Dashed lines show grid-scale mixing, dotted lines the sgs contribution, and full lines total mixing consisting of grid-scale plus sgs contribution.

the observed profile. The mesoscale simulation this time is in overall better agreement with the measured profile (FB $= 0.05$) compared to the CAIRDIO simulation (FB $= -0.40$), but likely only as a result of the overestimated PM_{10} background, which by chance matches the measured roadside profile in the temporal mean.

Concluding from this analysis, BC background concentrations are represented reasonably accurate in both the mesoscale CTM COSMO-MUSCAT and the urban-scale model CAIRDIO throughout the simulation period. In contrast, the more complex pollutant PM_{10} showed higher uncertainties and a considerable negative bias, and proofed therefore to be more complicated

https://doi.org/10.5194/gmd-2021-358
Preprint. Discussion started: 22 November 2021


Geoscientific Model Development Discussions

in the model study of the intra-urban air-pollution variability. As expected, the mesoscale model indiscriminately reproduced the background profiles at all sites, which results in a large model bias for the roadside stations, except for PM_{10} at the side LC. In comparison, the CAIRDIO simulation considered the influence of the local environment, as simulated roadside profiles show a much larger variability than the corresponding background profile. The model bias is within a moderately positive to moderately negative range at the roadside stations (except again for PM_{10} at side LC). For BC, this residual bias can be mostly attributed to individual misrepresented peaks in the simulation. Whether a horizontal grid spacing finer than $40\,\mathrm{m}$ can still improve model representation of roadside concentrations is explored within the framework of the subsequent sensitivity study.

3.3 Grid-size sensitivity

3.3.1 Planetary boundary layer and mixing

Before evaluating grid-size sensitivity of modeled air pollution at the air-monitoring sites, some of the most important variables characteristic to the PBL state are investigated in this paragraph. For this purpose, domain LE is simulated with horizontal grid spacings of $40\,\mathrm{m}$, $20\,\mathrm{m}$, $10\,\mathrm{m}$, and $5\,\mathrm{m}$. Note that due to imperfections with the offline-nesting, the $40\,\mathrm{m}$ resolution is repeated with the local domains for a more accurate comparison. Resolved fluxes of momentum and tracer concentration BC are computed by using corrected temporal samples to represent an ensemble averaging. Given a scalar variable c, each temporal snapshot c_i is corrected for horizontally-averaged changes throughout the averaging period consisting of n snapshots:

$$c_i^* = c_i - < c_i >_h + < c_0 >_h \; \forall i \in \{0,1,2,..,n\}, \tag{4}$$

where the brackets $<>_h$ denote for the horizontal averaging and c_i^* is the corrected snapshot. Note that the horizontal average within the canopy layer excludes the inaccessible grid-cell volume by using the volume-scaling field χ as weights. For the velocity components, the cell-face area scaling field $\boldsymbol{\eta}$ is used instead of χ. Vertical profiles of the computed horizontally and hourly averaged variables $\overline{u}$, $\overline{v}$, $\overline{\Theta_v}$, $\overline{c_{\mathrm{BC}}}$, $\overline{u'w'}$, $\overline{v'w'}$, and $\overline{c'_{\mathrm{BC}}w'}$ are depicted in Figure 14 for the two contrasting PBL states already discussed in Section 3.1. Starting with the first case on 2 March at 00:30 UTC, strong southerly winds along with a weakly stable stratification created a shear-driven, turbulent PBL. In the profiles of the mean horizontal wind components (Fig. 14a-b), grid sensitivity is mainly restricted to the first $20\,\mathrm{m}$ within the canopy layer. Inside there, the run with default grid-spacing of $40\,\mathrm{m}$ results in a slightly higher wind speed compared to the runs with a better resolution of buildings. Profiles of Θ_v show negligible sensitivity (Fig. 14c), while for scalar c_{BC} concentrations within the urban canopy are slightly higher in the $20\,\mathrm{m}$ and $10\,\mathrm{m}$ runs compared to the $40\,\mathrm{m}$ and $5\,\mathrm{m}$ runs (Fig. 14d). Significantly more sensitivity is observed in the vertical turbulent fluxes of momentum (Fig. 14e-g) and scalar BC (Fig. 14h). Although the subgrid-scale contributions (dotted lines) become larger as the resolution is decreased, they do not seem to compensate for the loss of resolved fluxes. Apparently, this issue is not restricted to the urban canopy, but may be influenced by an underestimation of vertical wind shear just above the roof tops in the coarser runs. Nevertheless, sensitivity in c_{BC} is very low, arguably because transport is mostly horizontal in the shear-driven case. Thus, the profiles of c_{BC} and $\overline{c'_{\mathrm{BC}}w'}$ are only weakly related to each other.

https://doi.org/10.5194/gmd-2021-358
Preprint. Discussion started: 22 November 2021


Geoscientific Model Development Discussions

For the featured convective case around 2 March 12:30 UTC, horizontal wind speeds are by one order of magnitude lower compared to the first case, but a positive vertical heat flux is responsible for turbulence generation this time. The averaged wind profiles (Fig. 14a-b) show a similar sensitivity to the already discussed shear-driven case, which may indeed indicate an increase of the prescribed roughness length of the subgrid-scale building structure for momentum transfer in future simulations with diffuse buildings. Compared to the shear-driven case, a more substantial sensitivity in Θ_v of approximately $0.5\,\mathrm{K}$ and also in c_{BC} can be observed for the height range within the urban canopy (Fig. 14k-i). In contrast, a negligible grid-sensitivity is observed for the vertical flux $\overline{c'_{BC}w'}$ across the full height range (Fig. 14q). The reason for this behavior in the given convective case is that scalar transport is dominated by vertical mixing. Since the emissions are constant in all simulations, also no variations in $\overline{c'_{BC}w'}$ are expected when assuming an equilibrium state. This, however, does not imply that the profiles of eddy diffusivity are constant across the simulations, as the vertical gradients in c_{BC} adjust to match the flux profile. In fact, there must be a significant sensitivity of the vertical eddy diffusivity within the height range where the scalar profiles start to diverge, which is not just by coincidence also the area with the largest instability (the largest super-adiabacity in Θ_v). In the currently used subgrid-scale model, the turbulent Prandtl number P_t, which relates the eddy diffusivity to the eddy viscosity, is not further decreased below the neutral value of 0.66 for unstable stratification. However, in unstable conditions P_t may be actually much lower, implying a larger eddy diffusivity. An adjustment of the stability-dependent P_t may be needed in future simulations.

3.3.2 Distribution of air pollutants

For the evaluation of grid sensitivity at the air-monitoring sites, the horizontal grid spacing of the locally nested domains centered at roadside-classified air-monitoring sites (LE, LL, or LC, respectively) is varied between $40\,\mathrm{m}$, $20\,\mathrm{m}$, $10\,\mathrm{m}$, and $5\,\mathrm{m}$. The finest resolution of $5\,\mathrm{m}$ permits conventional building-resolved simulations, but is omitted for the background stations LT and LW due to the expected low model sensitivity there. Model results are again hourly averaged and spatially interpolated to the exact locations of the measurement sites. In Figure 16, the obtained time series are plotted against each other and against the measurements as reference, similar to Fig. 13. In addition, the corresponding FB values in relation to the measurements are listed in Tab. 3. For the BC background station LT (Fig. 16a), little grid-size sensitivity is found as to expect. At best, BC peak concentrations around 1 March 18:00 UTC tend to be slightly higher with increased resolution, which is mainly from the sensitivity of the subgrid-scale parameterization, as the PBL was stably stratified during this time. FB varies only slightly from 0.05 to 0.00 for the $10\,\mathrm{m}$ grid spacing. More interesting are the results for the roadside station LE (Fig. 16b). For this site, the $40\,\mathrm{m}$ resolution resulted in an underestimation of BC peak concentrations. In fact, decreasing the grid spacing down to lower or equal $10\,\mathrm{m}$ results in a significant better representation of both evening rush-hour peaks. However, absolute peak concentrations still cannot be fully recovered. Interestingly, no further improvements can be achieved with the finest resolution of $5\,\mathrm{m}$. Aside from the discussed rush-hour peaks, model sensitivity is considerably lower, and it seems like the $10\,\mathrm{m}$ and $20\,\mathrm{m}$ grid spacings result in slightly higher concentrations compared to the $40\,\mathrm{m}$ and $5\,\mathrm{m}$ resolutions, which are close together. The improved peak representation results in a slightly lower model FB ranging from 0.06 to 0.16.

For the station LC (Fig. 16c), a distinction of the evening rush-hour peaks from the remaining time series turns out to be

https://doi.org/10.5194/gmd-2021-358
Preprint. Discussion started: 22 November 2021


Geoscientific Model Development Discussions
Open Access
EGU

reasonable too. For the two evening peaks, a decrease of peak BC concentrations with increasing spatial resolution can be observed, which is in contrast to the sensitivity at the station LE. A closer inspection of the spatial concentration gradients in Figure 15 reveals the reason for this contrasting sensitivity. The station LC lies next to two traffic lanes to the north in the model. In the $40\,\mathrm{m}$ run, the exhaust plumes spread over a comparatively large area, causing a smearing of the gradient in the vicinity of the air-monitoring site. In the $5\,\mathrm{m}$ run, spatial gradients near the road are much sharper, which places the measurement site mostly outside the exhaust plumes. It is, however, questionable if the line-source representation of traffic emissions is still adequate in combination with such a fine grid spacing, as in reality emissions can be effectively spread over a larger area by car-induced turbulence (Gross, 2016).

At the site LE, BC is directly measured above the traffic emissions. Here, the $40\,\mathrm{m}$ spatial resolution is too coarse to keep the air pollution trapped within the narrow street canyon, as also part of the emissions are emitted outside of the canyon. This explains the observed positive sensitivity of modeled peak BC concentration with increased resolution. Obviously, the $10\,\mathrm{m}$ grid spacing is already adequate to contain all of the traffic emissions within the canyon. The observed sensitivity at site LC for the rest of the simulation period is characterized by comparatively higher BC concentrations in the $20\,\mathrm{m}$ and also $10\,\mathrm{m}$ simulation compared to the $5\,\mathrm{m}$ $5\,\mathrm{m}$ and $40\,\mathrm{m}$ runs. This sensitivity can be attributed to the static subgrid-scale mixing length Δ_{sgs}. In the $40\,\mathrm{m}$ run, $\Delta_{sgs} = 20\,\mathrm{m}$ near the ground, which is about the typical height of buildings, and thus adequate when considering that the eddies within the urban canopy cannot be resolved. In the $20\,\mathrm{m}$ run, however, it is significantly smaller than building size, while there is still not enough resolution to capture the most important eddies. This likely results in an underestimation of vertical mixing within the urban canopy at such intermediate resolutions. By further decreasing the grid spacing down to $10\,\mathrm{m}$ or below, the largest eddies of the turbulent canopy flow are finally resolved.

Grid-sensitivity at the PM_{10}-measurement site LW is negligible (Fig. 16d), while it is again much more significant at the street-canyon site LL, where bulk PM_{10} is influenced to a large degree by traffic emissions. Not surprisingly, decreasing the grid spacing to $20\,\mathrm{m}$ results in higher modeled peak concentrations compared to the $40\,\mathrm{m}$ resolution. A further decrease of the grid spacing leads to some indecisive changes for the first evening peak and no significant changes for the second peak. As a result of the higher modeled peak concentrations in the higher resolved runs, an initially moderately positive FB $= 0.21$ of the $40\,\mathrm{m}$ is turned into slightly negative FB values ranging from -0.11 to -0.19. Finally at site LC, a quite similar behavior to the already discussed pollutant BC can be observed, albeit with an extenuated amplitude from the higher background influence of PM_{10}. Hence, FB varies only slightly between -0.46 and -0.32 for the set of sensitivity runs.

Having discussed in detail the grid-sensitivity of modeled BC and PM_{10} at the different measurement sites, it remains to quantify this sensitivity in proportion to the absolute simulation error in order to give a final conclusion. In addition, also the Pearson correlation coefficient r can serve as a criterion to judge the agreement of model results with observations. The model error ϵ is computed by following equation,

$$\epsilon = \frac{\sum_t \{|c_{mod} - c_{obs}|\}_t}{\sum_t \{c_{obs}\}_t} \times 100 \tag{5}$$

https://doi.org/10.5194/gmd-2021-358
Preprint. Discussion started: 22 November 2021

Geoscientific Model Development Discussions
Open Access
EGU

where c_{mod} and c_{obs} are the modeled and measured concentrations, respectively, and t is the time indexing. Both ϵ and r values computed for all sensitivity runs are additionally listed in Tab. 3. Based on these additional criteria, a large part of the mismatch between observations and measurements cannot be tackled by simply increasing the spatial resolution of the simulation. The largest error reduction and increase in r still results at the street-canyon sites. For example, the error of modeled BC concentrations at site LT is roughly one quarter lower in the $5\,\mathrm{m}$ simulation compared to the $40\,\mathrm{m}$ run. This suggests that grid spacing has the largest influence in close proximity to important pollution sources, like traffic. Still, the model error is dominated by other influences even there. At the other measurement sites this is even more so the case, as a relevant error reduction or increase in r cannot be observed when refining the grid. Concluding from these results, the benefits of an increase in spatial resolution beyond $40\,\mathrm{m}$ seem only minor in this limited modeling study. While in principle, processes can be resolved more accurately using a fine grid spacing, the potential advantages in real simulation studies are often scotched by the error from other processes, which are currently represented in a very simplified form in the model. For example, the emission model not only crudely simplifies the composition and spatial distribution of different emission types, but also their activation based on a smooth temporal profile, which cannot respond to locally deviating conditions.

	LT-BC	LE-BC	LC-BC	LW-PM_{10}	LL-PM_{10}	LC-PM_{10}
FB						
40 m	0.05	0.27	-0.19	-0.37	0.21	-0.36
20 m	0.01	**0.06**	-0.29	-0.38	**-0.11**	-0.46
10 m	**0.00**	**0.06**	-0.20	**-0.36**	-0.19	-0.41
5 m	-	0.16	**-0.05**	-	-0.14	**-0.32**
ϵ						
40 m	30.5	40.3	39.2	52.8	29.2	61.2
20 m	**30.2**	37.8	46.5	54.7	28.6	76.7
10 m	**30.2**	**30.4**	41.0	**52.6**	31.2	70.8
5 m	-	32.9	**35.1**	-	**27.8**	**60.0**
r						
40 m	**0.87**	0.88	**0.73**	**0.71**	0.66	**0.46**
20 m	0.86	0.84	0.70	0.69	0.73	0.19
10 m	**0.87**	**0.90**	0.70	0.68	**0.77**	0.17
5 m	-	**0.90**	0.68	-	**0.77**	0.29

Table 3. List of model to measurement FB, model error ϵ, and Pearson correlation coefficient r computed for all concentration time series of the performed sensitivity runs. The best-performing model resolution for each station and criterion, respectively, is highlighted in bold.

https://doi.org/10.5194/gmd-2021-358
Preprint. Discussion started: 22 November 2021


Geoscientific Model Development Discussions
Open Access
EGU

4 Conclusions

In this study, we applied the dispersion model CAIRDIO for the first time on a real mid-sized city to simulate dispersion of the pollutants PM_{10} and BC using a realistic meteorological setup, which was interpolated from a hosting mesoscale simulation. For the simulation period, two consecutive days in early March 2020 were selected. During this time, unsettled weather conditions with changing PBL characteristics and a generally pronounced magnitude of the intra-urban variability due to relatively low background pollution concentrations prevailed. The horizontal model resolution was set uniformly to $40\,\mathrm{m}$, which permits only to resolve the largest building structures, like industrial sites, while the majority of buildings within the city is described as diffuse obstacles. Nevertheless, the LES approach allows for an explicit representation of the most important turbulent PBL processes, which also include effects from a thermal surface forcing essential to the evolution of the PBL. This capability of the dynamical approach can be considered as a major advantage over more idealized models considering such effects, like stratification, only in parametric form (e.g. Gaussian plume or street-canyon models). In fact, the modeled PBL in this study showed turbulent features, which were consistent with the expected qualitative characteristics based on thermal stratification and vertical wind shear alone. Periods of intermittent or absent turbulence occurred when the critical gradient Richardson number was exceeded. The different dominating dispersion pathways during a specific PBL state (horizonal advection for shear-driven PBL vs. vertical turbulent mixing for convective PBL) resulted in visible qualitative differences in modeled near-surface BC concentrations, like a significantly higher background concentration and smoothed-out gradients in the shear-driven case compared to the convective case. The quantitative evaluation of modeled pollutant concentrations at the air-monitoring sites representative to the urban background showed a diurnal variability in modeled BC concentrations that was consistent with the measurements and thus provided further evidence for a realistic model representation of PBL transport processes. The model agreement with the measurements was also better for BC than PM_{10}, as BC is more locally influenced, while PM_{10} includes not only predominantly regional influences, but also uncertainties in the complex precursor chemistry. Ultimately, the model representation of the intra-urban variability of BC and PM_{10} concentrations was evaluated using the measurements at the road sites. These were distinct from the measurements at the background sites by the significantly elevated concentrations throughout daytime and the peaks from the traffic-rush hours. Here the model responded adequately to the different environment characterized by surrounding buildings and high localized traffic emissions, as it mostly reproduced the elevated concentrations. This was in strong contrast to the driving mesoscale simulation, which indiscriminately reproduced the background concentrations at all sites. While we did not directly apportion the effects of diffuse buildings in addition to the increased model resolution leading to these different model results, the performance of additional sensitivity runs using locally nested domains with increased horizontal grid resolution down to $5\,\mathrm{m}$ helped to shed some light on this aspect. While we did not observe much model sensitivity to grid resolution at the background sites, this was not the case at the roadside locations. Part of the observed sensitivity at the street-canyon sites could be explained by the simple fact that a spatial resolution of $40\,\mathrm{m}$ is not sufficient to contain the traffic emissions within the narrower street canyons. However, without the presence of buildings in the model, the emissions would have been diluted into a much larger air volume from the first place. At more open sites, the more pronounced horizontal smearing of pollution gradients with increased horizontal grid spacing resulted in an opposite sen-

https://doi.org/10.5194/gmd-2021-358
Preprint. Discussion started: 22 November 2021


Geoscientific Model Development Discussions

sitivity of modeled concentrations, as the air-monitoring sites are located outside the densest traffic-emission plumes in the $5\,\mathrm{m}$ run. Arguably, the sign of the sensitivity also depends on the distance to the nearby traffic lanes here. It is disputed, however, if the results with the finest grid spacing are more realistic, as turbulent diffusion might be underestimated by neglecting small scale processes like traffic motion. It became also apparent that buildings contribute importantly to turbulent vertical mixing within the roughness sublayer. When decreasing the grid spacing, these turbulent motions are successively better resolved. Especially in the shear-driven case, we observed a significant grid-size sensitivity of the vertical turbulent scalar flux just above the building roofs. The best explanation for the underestimation of this flux in the default $40\,\mathrm{m}$ simulation is a possible underestimation of the drag from diffuse buildings on the air flow, which would reduce vertical wind shear above the building roofs and also decrease the vertical turbulent flux in favor of the horizontal advective flux. In the convective case, grid-size sensitivity of domain-averaged near-surface BC concentrations could also be traced back to an underestimation of the parameterized vertical diffusivity, especially in the super-adiabatic height range induced from the surface-heat flux. Here, a possible mismatch of the parameterized turbulent Prandtl number was pointed out. In order to further corroborate the reasons behind the observed sensitivity in the vertical scalar fluxes, additional sensitivity runs with variations of the parameters in question (e.g. r_0, P_t) need to be carried out in future studies focusing mainly on such aspects. Also, we assumed the validity of the downscaled surface potential-temperature fields prescribed in the simulation, which affect also the heat flux from building surfaces, mainly in lack of a more physically-based alternative. Here, the further comparison with a microscale model equipped with an own radiation and surface scheme could provide confidence, which was however out of the scope of this study. Finally, in spite of the observed and discussed sensitivity, the comparison of the error in modeled concentrations at the measurement sites showed only slight improvements with an increasing grid resolution, if any at all. For a more significant model evaluation, definitely a more prolonged simulation period needs to be investigated. Still, the findings from this study point to the necessity of more accurately representing other non-physical components in the model, in order to benefit from a more accurate representation of model physics with building-resolving grids. Most notably to mention are the traffic emissions with their currently limited accuracy and comprehensiveness, which may be improved in future simulations with the incorporation of real-time traffic-flux data. Nevertheless, with the currently available data the showcased modeling approach performed at urban gray-zone horizontal resolutions showed to be a very promising tool for application on more targeted research questions that previously relied on mesoscale model outputs, like, e.g., urban population exposure to air pollution.

Code availability. The source code of CAIRDIO model version 2.0, as well as utilities for data pre-processing are accessible in release under the license GPL v3 and later at https://doi.org/10.5281/zenodo.5585383 (Weger et al., 2021b).

Data availability. The data used in this study, which include model results and air-monitoring observations in part provided by LfULG and TROPOS, are accessible at https://doi.org/10.5281/zenodo.5645267.

https://doi.org/10.5194/gmd-2021-358
Preprint. Discussion started: 22 November 2021

Geoscientific Model Development Discussions

Appendix A: CAIRDIO v2.0 improvements

The actual model version 2.0 used in this paper features additional improvements over the published version 1.0, which apply to several model components and are listed in the following.

A0.1 Revised advection scheme

In CAIRDIO v.1.0, advection used linear 5^{th}-order reconstructions with additional limiting for positive scalars. It is well known that such upwind-biased odd-order schemes result in numerical diffusion, as the leading error term is diffusive. In LES, numerical diffusion has a detrimental impact on the correct energy transfer, as excessive energy is drained from the smallest scales that feed on the larger eddies, thus affecting the entire energy cascade. The manifestation of excessive damping can be seen in the energy spectra of Figure A1. Nevertheless, some sort of numerical damping of the smallest wavelengths is necessary in order to maintain numerical stability, as these scales are flawed by large dispersion errors. Recognizing that the standard 5^{th}-order linear upwind formulation carried out in each dimension separately is simply the addition of a high-order diffusion term to a non-diffusive 6^{th}-order central scheme, directly leads to an opportunity to control numerical diffusion:

$$\partial_{adv}^{5\text{th}} = \partial_{adv}^{6\text{th}} + \nabla \cdot \left(\boldsymbol{u}_{+} \Delta_h \nabla^{5\text{th}} \right) \tag{A1}$$

Here, Δ_h is the grid spacing, $\boldsymbol{u}_{+}$ the positive definite transport velocity component, and $\nabla^{5\text{th}}$ a finite difference operator using 5^{th}-order reconstructions. The product $\boldsymbol{u}_{+}\Delta_h$ is called numerical diffusion coefficient, and mainly acts in the dominant transport direction. In the revised scheme, $\boldsymbol{u}_{+}$ is replaced by a constant parameter $d = 0.05$. Note that this results in isotropic diffusion, similar to the method proposed in Xue (2000) for high-order damping.

A0.2 Prognostic TKE formulation for subgrid-scale mixing

In version 1.0 an algebraic eddy-viscosity formulation was used. Therein, eddy viscosity was diagnosed from the strain-rate tensor $\boldsymbol{S}$ without taking buoyancy effects into account. In order to simulate non-neutral PBLs, we implemented a prognostic subgrid-scale TKE formulation similar to Deardorff 1973 in version 2.0. This scheme not only takes buoyancy effects into account but also avoids the local-equilibrium assumption and thus may provide more accurate results with coarse grid spacings. The prognostic equation for subgrid-scale TKE is given by

$$\partial_t e = -\nabla \left(\boldsymbol{u} e \right) + 2 \nabla k_h \nabla e + 2 k_m |\boldsymbol{S}|^2 - k_h N_c^2 - \frac{c_\epsilon}{l_{sgs}} e^{3/2}. \tag{A2}$$

The first two terms correspond to the advective-diffusive transport, which also incorporate the pressure-correlation term parameterized by a doubling of the diffusive flux. The shear-production term is parameterized with the squared magnitude of

https://doi.org/10.5194/gmd-2021-358
Preprint. Discussion started: 22 November 2021


Geoscientific Model Development Discussions

$\boldsymbol{S}$ and the buoyancy-production term results from the squared Brunt–Väisälä frequency N_c multiplied with the eddy diffusivity k_c. Finally, the dissipation term contains a stability-dependent subgrid-mixing length, which is formulated by

$$l_{sgs} = \min\left(\Delta, 0.76\sqrt{e}/N_c\right), \tag{A3}$$

where $\Delta = (\Delta_x \Delta_y \Delta_z)^{1/3}$ is the static (grid) mixing length. The eddy viscosity coefficient k_m is parameterized according to:

$$k_m = c_m \sqrt{e} \Delta \tag{A4}$$

Note that we replaced l_{sgs} with Δ therein, as the original formulation resulted in a too small eddy diffusivity for stable stratifications within the roughness sublayer of diffuse urban canopies. We argue that in such a case, the mixing length is always at least as large as the typical building height, and thus not really stability dependent therein. c_m and c_e are model constants, and can be related to the static Smagorinsky constant by $c_s = c_m^{3/4}/c_e^{1/4}$. Fixing the value of $c_e = 0.93$, the constant c_m is then determined by the choice of c_s. Thus, c_s is retained as the same model parameter used in the diagnostic scheme.

Lastly, the eddy diffusivity k_h for heat and scalar transport is related to k_m by the inverse turbulent Prandtl number:

$$k_h = Pr_t^{-1} k_m \tag{A5}$$

In Deardorff (1973), Pr_t^{-1} is parameterized according to

$$Pr_t^{-1} = 1 + 2\frac{l_{sgs}}{\Delta}. \tag{A6}$$

However, as pointed out in paragraph 3.3.1, the neutral value of Pr_t^{-1} may be too low in unstable conditions (cf. Li et al. 2015), and if a negative impact from this is further corroborated, the stability dependency will be entirely replaced by another formulation in a future model version.

A0.3 Dry and wet deposition of particulate matter

For a consistent model description of particulate matter dispersion, dry and wet deposition processes are considered too in the new model version 2.0. For dry deposition, the scheme of Zhang and He (2014) was implemented, which considers the bulk-size categories $PM_{2.5}$, $PM_{2.5-10}$ and PM_{10+}. Accordingly, the deposition flux of a given particle category on a horizontal surface is given by the particle mass concentration c_{pm} times the parameterized deposition velocity v_d, which contains the contributions from gravitational settling v_g, aerodynamic resistance r_a and surface resistance r_s:

$$v_d = v_g + \frac{1}{r_a + r_s} \tag{A7}$$

https://doi.org/10.5194/gmd-2021-358
Preprint. Discussion started: 22 November 2021


Geoscientific Model Development Discussions

v_g primarily depends on particle size and can thus be set to a constant. For $PM_{2.5-10}$ a value of $10^{-4}\,\mathrm{m\,s^{-1}}$ is used, while for $PM_{2.5}$ gravitational settling is neglected. The aerodynamic resistance is computed according to

$$r_a = \frac{2}{3u_* t_h}, \tag{A8}$$

where u_* is the friction velocity and t_h the surface-transfer coefficient for heat, also used in the parameterization of heat and moisture fluxes. Finally, Zhang and He (2014) provide empirical relationships for the surface-depostion velocity v_{ds}, which is the inverse of r_s. For $PM_{2.5}$, a linear dependency on u_* is assumed

$$v_{ds} = a_1 u_*, \tag{A9}$$

while $PM_{2.5-10}$ uses a cubic formula for land-use classes with constant leaf-area index:

$$v_{ds} = b_1 u_* + b_2 u_*^2 + b_3 u_*^3. \tag{A10}$$

The coefficients a_1, b_1, b_2, and b_3 are adjusted to the different land-use classes considered by the scheme. To obtain the final deposition tendency, the computed deposition fluxes for each relevant land-use class are multiplied with respective surface area and summed up.

Since clouds are not computed in CAIRDIO, wet deposition is solely based on sub-cloud scavenging (also precipitation scavenging), for which precipitation rates pr $[\mathrm{kg\,m^{-2}\,s^{-1}}]$ of the mesoscale host simulation are inferred from. It is assumed that throughout the simulated vertical range of the PBL, the precipitation rate is constant. As for the scavenging coefficients, $0.104\,\mathrm{m^2\,kg^{-1}}$ and $0.418\,\mathrm{m^2\,kg^{-1}}$ are assumed for the categories $PM_{2.5}$ and $PM_{2.5-10}$, respectively.

Author contributions. Michael Weger contributed in the development of the model setups, the execution and evaluation of model runs, as well as in paper writing. Bernd Heinold provided technical assistance and assistance regarding the study content, as well as for paper writing and proof reading. Alfred Wiedensohler and Maik Merkel provided the BC measurements for model validation.

Competing interests. All authors declare that they have no competing interests.

Acknowledgements. Recent German-wide emission data were provided by the Umweltbundesamt (UBA). We thank Mario Anhalt from the municipality of Leipzig for providing us with accurate traffic emissions for Leipzig. PM_{10} measurements were provided by the Sächsisches

https://doi.org/10.5194/gmd-2021-358
Preprint. Discussion started: 22 November 2021

Geoscientific Model Development Discussions

Landesamt für Umwelt, Landwirtschaft und Geologie (LfULG). Building geometries and orography (DGM1) are available from the Staatsbetrieb Geobasisinformation und Vermessung Sachsen (GeoSN). We thank the Deutscher Wetterdienst (DWD) for good cooperation and support.

https://doi.org/10.5194/gmd-2021-358
Preprint. Discussion started: 22 November 2021

References

Product Specification TEOM1405 Ambient Particulate Matter Monitor, Thermo Fisher Scientific Inc., https://www.thermofisher.com/document-connect/document-connect.html?url=https://assets.thermofisher.com/TFS-Assets%2FCAD%2FSpecification-Sheets%2FD19416.pdf, (last access: 02.11.2021), 2019.

Auguste, F., Lac, C., Masson, V., and Cariolle, D.: Large-Eddy Simulations with an Immersed Boundary Method: Pollutant Dispersion over Urban Terrain, Atmosphere, 11, 113–135, doi:10.3390/atmos11010113, 2020.

Banzhaf, E. and Kollai, H.: Land use / Land cover for Leipzig, Germany, for 2012 by an object-based image analysis (OBIA), doi=10.1594/PANGAEA.895391, 2018.

Brown, M. J., Williams, M. D., Nelson, M. A., and Werley, K. A.: QUIC Transport and Dispersion Modeling of Vehicle Emissions in Cities for Better Public Health Assessments., Environmental health insights, 9, 55–65, doi:10.4137/EHI.S15662, 2015.

Burnett, R., Chen, H., Szyszkowicz, M., Fann, N., Hubbell, B., Pope, C. A., Apte, J. S., Brauer, M., Cohen, A., Weichenthal, S., Coggins, J., Di, Q., Brunekreef, B., Frostad, J., Lim, S. S., Kan, H., Walker, K. D., Thurston, G. D., Hayes, R. B., Lim, C. C., Turner, M. C., Jerrett, M., Krewski, D., Gapstur, S. M., Diver, W. R., Ostro, B., Goldberg, D., Crouse, D. L., Martin, R. V., Peters, P., Pinault, L., Tjepkema, M., van Donkelaar, A., Villeneuve, P. J., Miller, A. B., Yin, P., Zhou, M., Wang, L., Janssen, N. A. H., Marra, M., Atkinson, R. W., Tsang, H., Quoc Thach, T., Cannon, J. B., Allen, R. T., Hart, J. E., Laden, F., Cesaroni, G., Forastiere, F., Weinmayr, G., Jaensch, A., Nagel, G., Concin, H., and Spadaro, J. V.: Global estimates of mortality associated with long-term exposure to outdoor fine particulate matter, Proceedings of the National Academy of Sciences, 115, 9592–9597, doi:10.1073/pnas.1803222115, 2018.

Cames, M. and Eckard, H.: Critical evaluation of the European diesel car boom - global comparison, environmental effects and various national strategies, Environmental Sciences Europe, 25, 15–37, doi:10.1186/2190-4715-25-15, 2013.

Coceal, O., Goulart, E. V., Branford, S., Glyn, T. T., and Belcher, S. E.: Flow structure and near-field dispersion in arrays of building-like obstacles, Journal of Wind Engineering and Industrial Aerodynamics, 125, 52–68, doi:10.1016/j.jweia.2013.11.013, 2014.

Deardorff, J. W.: The Use of Subgrid Transport Equations in a Three-Dimensional Model of Atmospheric Turbulence, Journal of Fluids Engineering, 95, 429–438, doi:10.1115/1.3447047, 1973.

Flemming, J., Huijnen, V., Arteta, J., Bechtold, P., Beljaars, A., Blechschmidt, A.-M., Diamantakis, M., Engelen, R., Gaude, A., Inness, A., Jones, L., Peuch, V.-H., Schulz, M., Stein, O., and Tsikerdekis, A.: Tropospheric chemistry in the Integrated Forecasting System of ECMWF, https://www.ecmwf.int/node/9426, doi:10.21957/kkljbmrkh, 2014.

Foroutan, H., Tang, W., Heist, D. K., Perry, S. G., Brouwer, L. H., and Monbureau, E. M.: Numerical analysis of pollutant dispersion around elongated buildings: an embedded large eddy simulation approach, Atmospheric environment, 187, 117–130, doi:10.1016/j.atmosenv.2018.05.053, 2018.

Forster, P., Forster, H., Evans, M., Gidden, M., Jones, C., Keller, C., Lamboll, R., Quéré, C., Rogelj, J., Rosen, D., Schleussner, C., Richardson, T., Smith, C., and Turnock, S.: Current and future global climate impacts resulting from COVID-19, Nature Climate Change, 10, 913–919, doi:10.1038/s41558-020-0883-0, 2020.

Fuka, V., Xie, Z.-T., Castro, I. P., Hayden, P., Carpentieri, M., and Robins, A. G.: Scalar fluxes near a tall building in an aligned array of rectangular buildings, Boundary-Layer Meteorology, 167, 53–76, doi:10.1007/s10546-017-0308-4, 2018.

Google-LLC: Google COVID-19 Community Mobility Reports, https://www.google.com/covid19/mobility/, (last access: 02.09.2021), 2020.

Goulart, E., Reis, N., Lavor, V., Castro, I., Santos, J., and Xie, Z.: Local and non-local effects of building arrangements on pollutant fluxes within the urban canopy, Building and Environment, 147, 23–34, doi:10.1016/j.buildenv.2018.09.023, 2019.

https://doi.org/10.5194/gmd-2021-358
Preprint. Discussion started: 22 November 2021

Goulart, E. V., Coceal, O., and Belcher, S. E.: Dispersion of a passive scalar within and above an urban street network, Boundary-Layer Meteorology, 166, 351–366, doi:10.1007/s10546-017-0315-5, 2018.

Gross, G.: Dispersion of traffic exhausts emitted from a stationary line source versus individual moving cars - a numerical comparison, Meteorologische Zeitschrift, 25, 479–487, doi:10.1127/metz/2016/0797, 2016.

Heinold, B., Weger, M., Knoth, O., Schrödner, R., Müller, T., and Tonisson, L.: High-resolution air-quality modeling in urban areas -A case study for the City of Leipzig, Proceedings of the 37th International Technical Meeting on Air Pollution Modelling and its Application, Hamburg, Germany, 23 - 27 September, 2019, 2019.

Hertwig, D., Grimmond, S., Kotthaus, S., Vanderwel, C., Gough, H., Haeffelin, M., and Robins, A.: Variability of physical meteorology in urban areas at different scales: implications for air quality, Faraday Discussions, 226, 149–172, doi:10.1039/D0FD00098A, 2021.

Higson, H., Griffiths, R., Jones, C., and Hall, D.: Flow and dispersion around an isolated building, Atmospheric Environment, 30, 2859–2870, doi:10.1016/1352-2310(95)00313-4, 1996.

Jiang, G. and Yoshie, R.: Side ratio effects on flow and pollutant dispersion around an isolated high-rise building in a turbulent boundary layer, Building and Environment, 180, 107 078, doi:10.1016/j.buildenv.2020.107078, 2020.

Klose, S., Birmili, W., Voigtländer, J., Tuch, T., Wehner, B., Wiedensohler, A., and Ketzel, M.: Particle number emissions of motor traffic derived from street canyon measurements in a Central European city, Atmospheric Chemistry and Physics Discussions, 9, 3763–3809, doi:10.5194/acpd-9-3763-2009, 2009.

Korhonen, A., Lehtomäki, H., Rumrich, I., Karvosenoja, N., Paunu, V.-V., Kupiainen, K., Sofiev, M., Palamarchuk, Y., Kukkonen, J., Kangas, L., Karppinen, A., and Hänninen, O.: Influence of spatial resolution on population PM2.5 exposure and health impacts, Air Quality, Atmosphere Health, 12, 705–718, doi:10.1007/s11869-019-00690-z, 2019.

Kotthaus, S. and Grimmond, C.: Energy exchange in a dense urban environment – Part I: Temporal variability of long-term observations in central London, Urban Climate, 10, 261–280, iCUC8: The 8th International Conference on Urban Climate and the 10th Symposium on the Urban Environment, 2014.

Kuenen, J. J. P., Visschedijk, A. J. H., Jozwicka, M., and Denier van der Gon, H. A. C.: TNO-MACC_II emission inventory; a multi-year (2003–2009) consistent high-resolution European emission inventory for air quality modelling, Atmospheric Chemistry and Physics, 14, 10 963–10 976, doi:10.5194/acp-14-10963-2014, 2014.

Li, D., Katul, G., and Zilitinkevich, S.: Revisiting the turbulent Prandtl number in an idealized atmospheric surface layer, Journal of the Atmospheric Sciences, 72, 2394–2410, doi:10.1175/JAS-D-14-0335.1, 2015.

Louka, P., Vachon, G., Sini, J.-F., Mestayer, P. G., and Rosant, J.-M.: Thermal effects on the airflow in a street canyon – Nantes'99 experimental results, Water, Air and Soil Pollution: Focus, 2, 351–364, doi:10.1023/A:1021355906101, 2002.

Makedonas, A., Carpentieri, M., and Placidi, M.: Urban boundary layers over dense and tall canopies, Boundary-Layer Meteorology, 181, 73–93, doi:10.1007/s10546-021-00635-z, 2021.

Martilli, A., Clappier, A., and Rotach, M.: An urban surface exchange parameterisation for mesoscale models, Boundary-Layer Meteorology, 104, 261–304, doi:10.1023/A:1016099921195, 2002.

Marucci, D. and Carpentieri, M.: Effect of local and upwind stratification on flow and dispersion inside and above a bi-dimensional street canyon, Building and Environment, 156, 74–88, doi:10.1016/j.buildenv.2019.04.013, 2019.

Ortiz, A. and Guerreiro, C.: Air Quality in Europe - 2020 report, doi:10.2800/786656, 2020.

Page, S. J., Tuchman, D. P., and Vinson, R. P.: Thermally induced filter bias in TEOM mass measurement, Journal of Environmental Monitoring, 9, 760–767, doi:"10.1039/B704424K, 2007.

https://doi.org/10.5194/gmd-2021-358
Preprint. Discussion started: 22 November 2021

Park, M., Joo, H. S., Lee, K., Jang, M., Kim, S. D., Kim, I., Borlaza, L. J. S., Lim, H., Shin, H., Chung, K. H., Choi, Y.-H., Park, S. G., Bae, M.-S., Lee, J., Song, H., and Park, K.: Differential toxicities of fine particulate matters from various sources, Scientific Reports, 8, 17 007 – 17 018, doi:10.1038/s41598-018-35398-0, 2018.

Park, S.-J., Choi, W., Kim, J.-J., Kim, M. J., Park, R. J., Han, K.-S., and Kang, G.: Effects of building–roof cooling on the flow and dispersion of reactive pollutants in an idealized urban street canyon, Building and Environment, 109, 175–189, doi:10.1016/j.buildenv.2016.09.011, 2016.

Petzold, A. and Schönlinner, M.: Multi-angle absorption photometry—a new method for the measurement of aerosol light absorption and atmospheric black carbon, Journal of Aerosol Science, 35, 421–441, doi:10.1016/j.jaerosci.2003.09.005, 2004.

Pflugmacher, D., Rabe, A., Peters, M., and Hostert, P.: Pan-European land cover map of 2015 based on Landsat and LUCAS data, doi:10.1594/PANGAEA.896282, 2018.

Roth, M.: Review of atmospheric turbulence over cities, Quarterly Journal of the Royal Meteorological Society, 126, 941–990, doi:10.1002/qj.49712656409, 2000.

Schubert, S., Grossman-Clarke, S., and Martilli, A.: A double-canyon radiation scheme for multi-layer urban canopy models, Boundary-Layer Meteorology, 145, 439–468, doi:10.1007/s10546-012-9728-3, 2012.

Schulzweida, U.: CDO User Guide, doi:10.5281/zenodo.3539275, 2019.

Sicard, P., Agathokleous, E., De Marco, A., Paoletti, E., and Calatayud, V.: Urban population exposure to air pollution in Europe over the last decades, Environmental Sciences Europe, 33, 15–37, doi:10.1186/s12302-020-00450-2, 2021.

Stockwell, W. R., Kirchner, F., Kuhn, M., and Seefeld, S.: A new mechanism for regional atmospheric chemistry modeling, Journal of Geophysical Research: Atmospheres, 102, 25 847–25 879, doi:10.1029/97JD00849, 1997.

Taraborrelli, D., Lawrence, M. G., Butler, T. M., Sander, R., and Lelieveld, J.: Mainz Isoprene Mechanism 2 (MIM2): an isoprene oxidation mechanism for regional and global atmospheric modelling, Atmospheric Chemistry and Physics, 9, 2751–2777, doi:10.5194/acp-9-2751-2009, 2009.

Tarín-Carrasco, P., Im, U., Geels, C., Palacios-Peña, L., and Jiménez-Guerrero, P.: Contribution of fine particulate matter to present and future premature mortality over Europe: A non-linear response, Environment International, 153, 106 517–106 530, doi:10.1016/j.envint.2021.106517, 2021.

Tõnisson, L., Voigtländer, J., Weger, M., Assmann, D., Käthner, R., Heinold, B., and Macke, A.: Knowledge transfer with citizen science: Luft-Leipzig case study, Sustainability, 13, 7855–7873, doi:10.3390/su13147855, 2021.

Vohra, K., Vodonos, A., Schwartz, J., Marais, E. A., Sulprizio, M. P., and Mickley, L. J.: Global mortality from outdoor fine particle pollution generated by fossil fuel combustion: Results from GEOS-Chem, Environmental Research, 195, 110 754, doi:10.1016/j.envres.2021.110754, 2021.

Weger, M., Knoth, O., and Heinold, B.: An urban large-eddy-simulation-based dispersion model for marginal grid resolutions: CAIRDIO v1.0, Geoscientific Model Development, 14, 1469–1492, doi:10.5194/gmd-14-1469-2021, 2021a.

Weger, M., Knoth, O., and Heinold, B.: CAIRDIO City-Scale Air Dispersion Model with Diffusive Obstacles [computer program], doi:10.5281/zenodo.5585383, 2021b.

Wiesner, A., Pfeifer, S., Merkel, M., Tuch, T., Weinhold, K., and Wiedensohler, A.: Real world vehicle emission factors for black carbon derived from longterm in-situ measurements and inverse modelling, Atmosphere, 12, doi:10.3390/atmos12010031, 2021.

https://doi.org/10.5194/gmd-2021-358
Preprint. Discussion started: 22 November 2021

Wolke, R., Schröder, W., Schrödner, R., and Renner, E.: Influence of grid resolution and meteorological forcing on simulated European air quality: A sensitivity study with the modeling system COSMO-MUSCAT, Atmospheric Environment, 53, 110 – 130, doi:doi.org/10.1016/j.atmosenv.2012.02.085, 2012.

Wu, H., Reis, S., Lin, C., Beverland, I. J., and Heal, M. R.: Identifying drivers for the intra-urban spatial variability of airborne particulate matter components and their interrelationships, Atmospheric Environment, 112, 306–316, doi:10.1016/j.atmosenv.2015.04.059, 2015.

Xue, M.: High-order monotonic numerical diffusion and smoothing, Monthly Weather Review, 128, 2853–2864, doi:10.1175/1520-0493(2000)128<2853:HOMNDA>2.0.CO;2, 2000.

Yalla, G. R., Oliver, T. A., and Moser, R. D.: Numerical dispersion effects on the energy cascade in large-eddy simulation, Physical Review Fluids, 6, L092 601, doi:10.1103/PhysRevFluids.6.L092601, 2021.

Ying, Q., Zhang, J., Zhang, H., Hu, J., and Kleeman, M. J.: Atmospheric age distribution of primary and secondary inorganic aerosols in a polluted atmosphere, American Chemical Society, 55, 5668–5676, doi:10.1021/acs.est.0c07334, 2021.

Zhang, L. and He, Z.: Technical Note: An empirical algorithm estimating dry deposition velocity of fine, coarse and giant particles, Atmospheric Chemistry and Physics, 14, 3729–3737, doi:10.5194/acp-14-3729-2014, 2014.

Zängl, G., Reinert, D., Rípodas, P., and Baldauf, M.: The ICON (ICOsahedral Non-hydrostatic) modelling framework of DWD and MPI-M: Description of the non-hydrostatic dynamical core, Quarterly Journal of the Royal Meteorological Society, 141, 563–579, doi:10.1002/qj.2378, 2015.

https://doi.org/10.5194/gmd-2021-358
Preprint. Discussion started: 22 November 2021

Geoscientific Model Development Discussions
Open Access
EGU

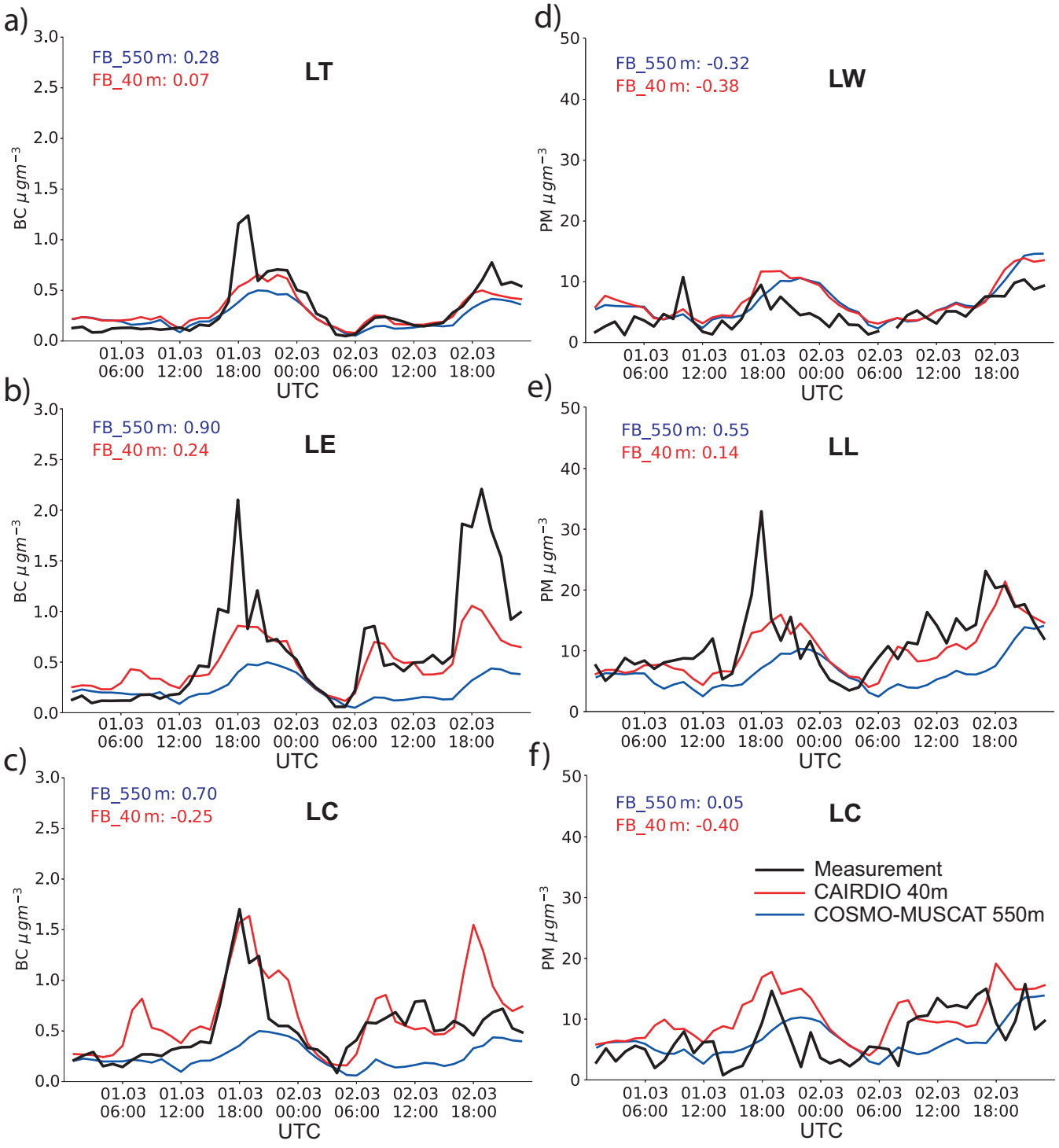

Figure 13. Comparison of measured BC concentrations (black lines) at the sites LE (a), LC (b), and LT (c) with simulation results of CAIRDIO (red lines) and COSMO-MUSCAT (blue lines). Respective profiles for PM_{10} are shown for the sites LL (d), LC (e), and LW (f). Additionally shown are temporally averaged fractional bias (FB) values in relation to measurements for all model runs.

https://doi.org/10.5194/gmd-2021-358
Preprint. Discussion started: 22 November 2021

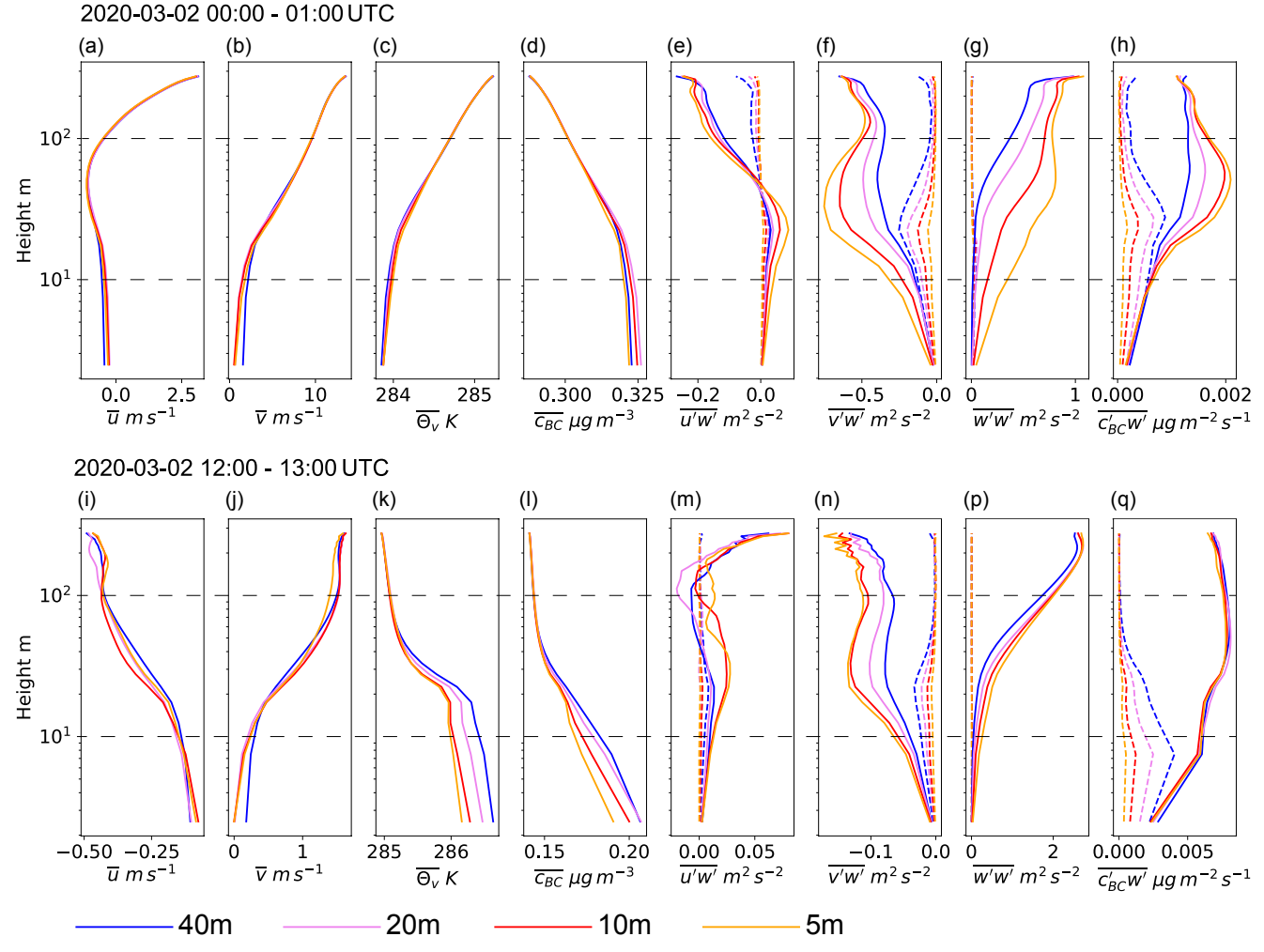

Figure 14. Vertical plots of horizontally averaged statistics for two different dates: Velocity components u (a, j) and v (b, k), virtual potential temperature (c, l), Richardson number (d, m), concentration of BC (e, n), and the turbulent statistics for vertical mixing of momentum (f, g, h, o, p, q) and BC (i, r), respectively. For the turbulent statistics, dashed lines are for the subgrid-scale (sgs) contribution, while the solid lines show both the sgs and grid scale contributions.

https://doi.org/10.5194/gmd-2021-358
Preprint. Discussion started: 22 November 2021

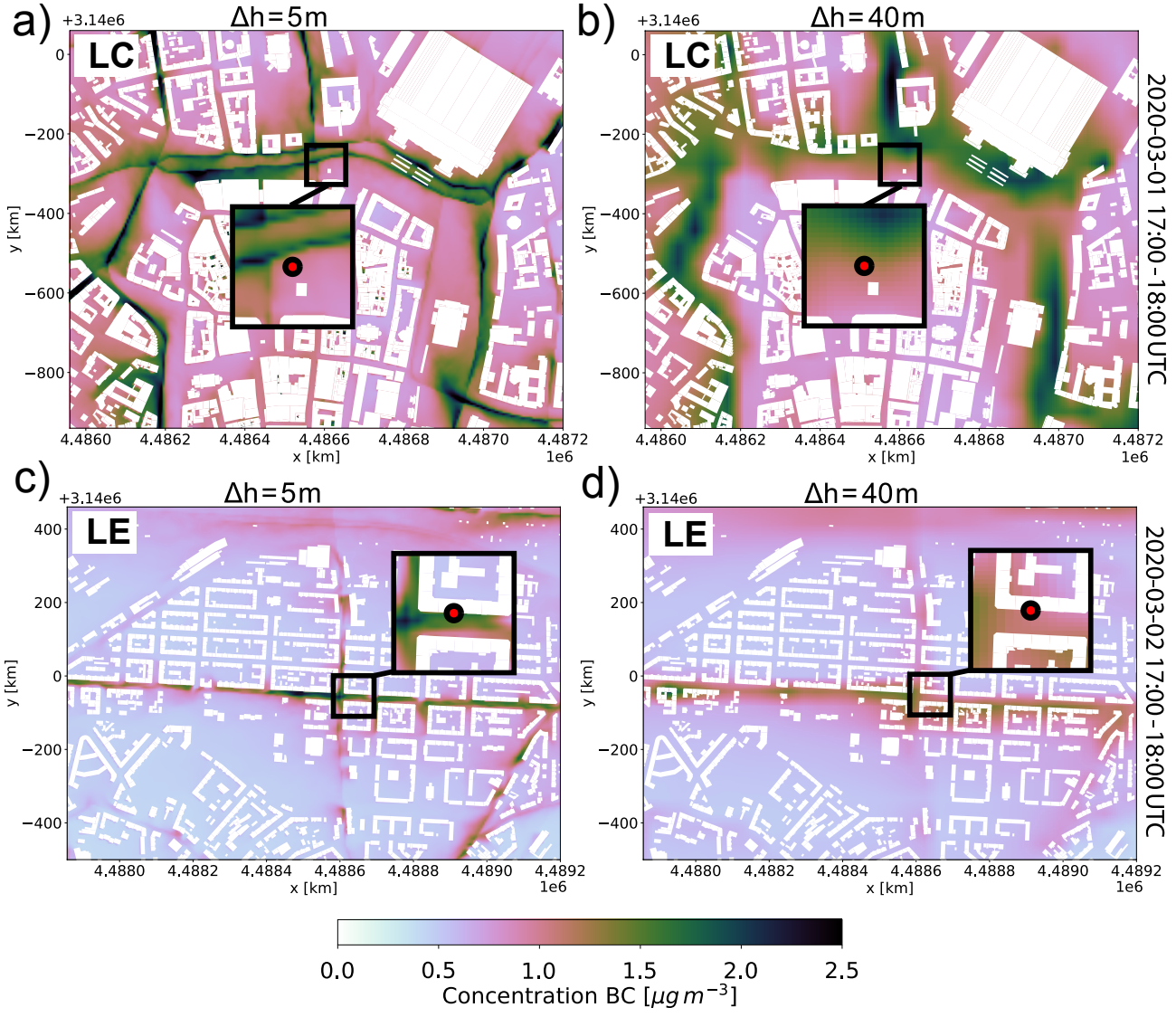

Figure 15. Qualitative comparison of the spatial distribution of modeled BC between the finest tested horizontal grid spacing of 5 m (a) and the default 40 m (b) with domain LC. Model results are temporally averaged for the rush-hour period on the evening of 1 March, and spatially interpolated at the height of corresponding air-monitoring site. In the locally magnified view of the insets, the air monitoring site is marked by a black circle. In (c) and (d) a similar comparison is shown with domain LE featuring the second rush-hour peak in the evening of 2 March.

https://doi.org/10.5194/gmd-2021-358
Preprint. Discussion started: 22 November 2021

Geoscientific Model Development Discussions
Open Access
EGU

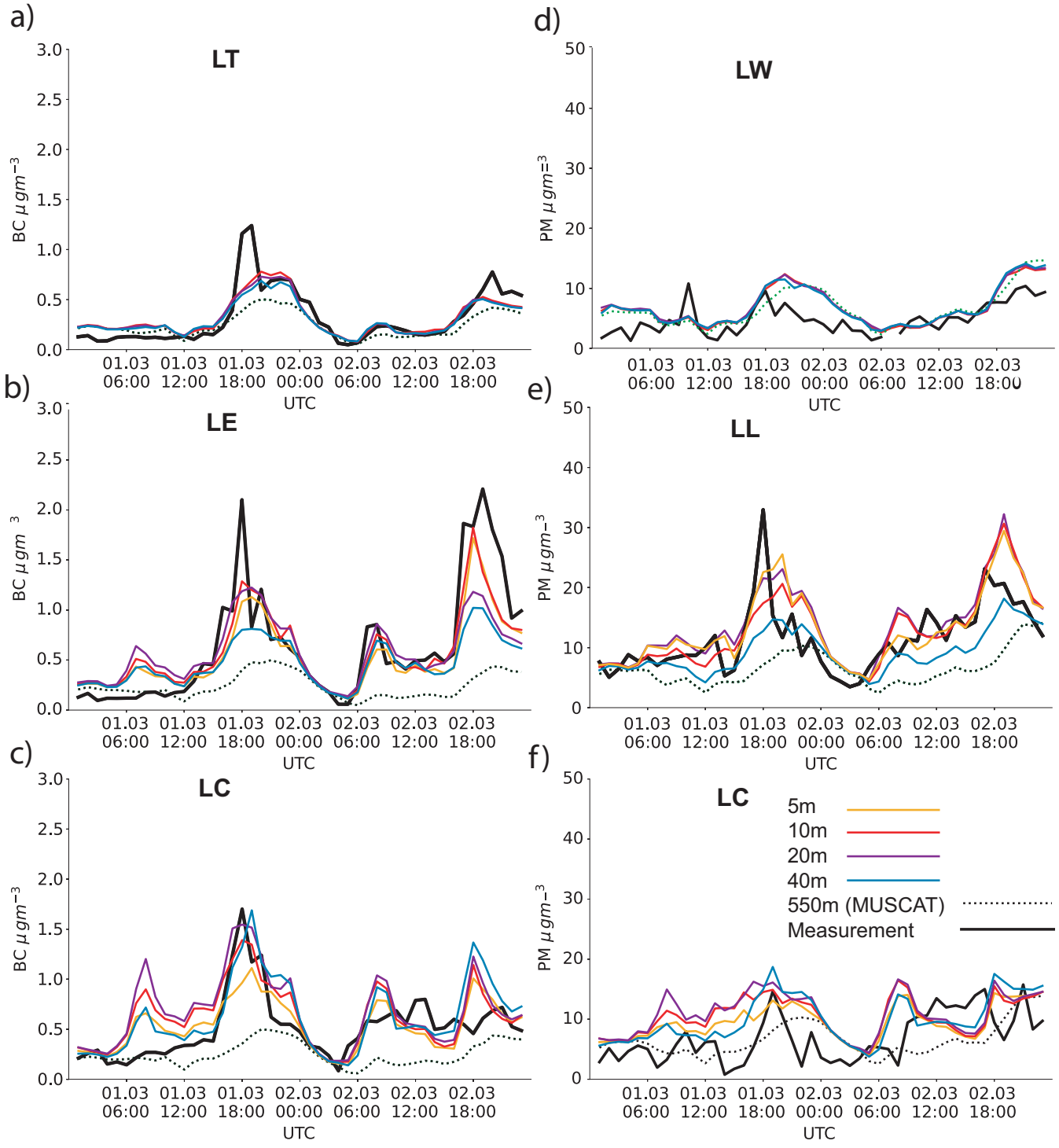

Figure 16. As Fig. 13, but showing the results of model sensitivity to the grid spacing. Compared are the nested CAIRDIO simulations with horizontal resolutions of 40 m, 20 m, 10 m, and 5 m, respectively, as well as the COSMO-MUSCAT simulation with 550 m horizontal resolution.

https://doi.org/10.5194/gmd-2021-358
Preprint. Discussion started: 22 November 2021

Geoscientific Model Development Discussions
Open Access
EGU

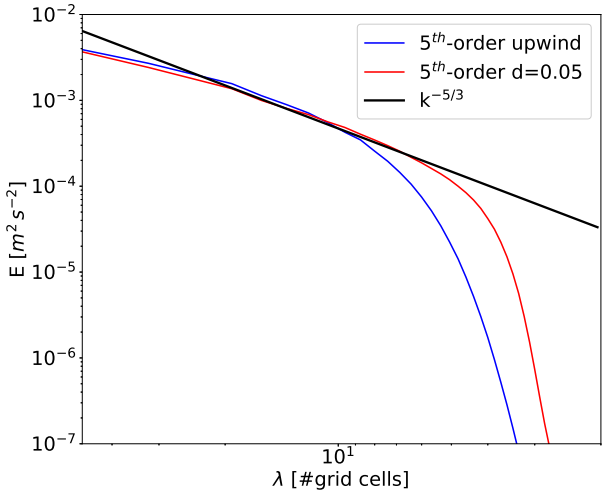

Figure A1. Developed energy-spectra in the flow-parallel direction for simulations of decaying isotropic turbulence with a superimposed translation velocity of similar magnitude as the turbulent fluctuations. The energy spectra are influenced by both the diffusive and dispersive errors of the advection scheme.